NANOPARTICLES AS CONTRAST AGENTS IN HIGH FREQUENCY ULTRASOUND IMAGING FOR PATHOLOGY DIAGNOSTICS

HANNAH WILKES

A thesis submitted to the University of Huddersfield in partial fulfilment of the requirements for the degree of Master of Science by research

The University of Huddersfield in collaboration with the National Physical Laboratory

January 2020

Acknowledgements

Firstly, I would like to thank my supervisor, Dr Lande Liu, whose expertise were invaluable in the formulation of this research topic and methodology.

I would also like to thank the research staff, particularly Dr Mark Hodnett at the ultrasound and under water acoustic department at the National Physical Laboratory, Teddington, for their support throughout this work.

I am also grateful for the support of our technical staff in the School of Applied Sciences, including Hayley Markham and Jack Edwards.

Lastly, I would also like to acknowledge a fellow student at the University of Huddersfield, Jason Bolton for helping with my experiments in this work.

Abstract

With high cancer survival rates been so often dependent on earlier detection, molecular imaging presents a particularly useful approach in cancer screening. However, the current imaging technology required to carry out such detailed examinations often involves the use of harmful radiation and/or very expensive equipment. Therefore, the demand for a new non-invasive and inexpensive imaging modality that is safe enough to allow for more frequent screening to take place (both before and after cancer treatment) continues to be of great importance (Buccafusca, Proserpio, Tralongo, Rametta Giuliano, & Tralongo, 2019).

High frequency ultrasound imaging is a non-invasive, non-ionising, portable and inexpensive imaging modality that can be used in conjunction with small diameter nanoparticles (10-100 nm) to move ultrasound imaging from the restrictions of the blood pool into small tumour masses.

Silica nanoparticles between 10-100nm in diameter were employed in this work to investigate the specific acoustic properties of silica nanoparticle material. The particle size distribution of the particles within a tissue mimic was characterised and acoustic measurements were taken using a 50MHz broadband transducer. The ultrasound attenuation data acquired in this work was not indicative of any relationship between the specific material properties of the silica nanoparticles employed and high frequency ultrasound. However, the development of the early stage experimental design outlined in this work provides a basis for future research and development in nanoparticle size characterisation within tissue mimics.

Table of Contents

Chapter 1: Contrast Enhanced Diagnostic Imaging: Towards Safer and More Cost-Effective Population Screening

1.1 Submicron contrast enhancing nanoparticles (<100 nm dia.), a neglected but important aspect of contrast enhanced ultrasound imaging.

The International Agency for Research on Cancer reported 9.6 million deaths from cancer in 2018 (IARC, 2018). An estimation of cancer survival rates of the most commonly occurring cancers, as provided by the Office for National Statistics anticipatedly revealed the survival rates of most cancers to be significantly increased if the cancer is detected at its early stage (Hawkes, 2019). In Hawkes (2019), results of the National Statistics report are reviewed to reveal that the highest one year cancer survival rates are found in melanoma, prostate cancer and breast cancer; which is largely due to the high percentage of prostate cancer and breast cancer being diagnosed at early stages (Agide, Sadeghi, Garmaroudi, & Tigabu, 2018; Hall, Schulthsiss, Farino, & Wong, 2015). Although breast cancer carries a high chance of been curable if detected in its early stages, breast cancer continues to be one of the biggest causes of cancer deaths worldwide (WHO, 2008). Liver, lung and colorectal cancers were all found to have one year survival rates that dropped significantly between detection at stage 1 and detection at stage 4 however, almost half of all lung cancers are not diagnosed before it has reached the most advanced stages (Hawkes, 2019). The most extreme decline in survival rates was found to be in liver cancers that are diagnosed between stage 2 (69.1% one year survival rate) and stage 3 (39.4% one year survival rate) (Hawkes, 2019) allowing hepatocellular carcinoma (HCC) to take its place as the third biggest cancer killer in the world (WHO, 2008). However, improved screening methods such as those described by Poustchi et al. (2011) highlight an opportunity to reduce the rate of mortality from HCC by increasing the frequency of screening procedures. Indeed, it can be deduced that most commonly occurring cancers would carry a higher chance of survival if physicians were able to diagnoses disease in its earlies stages, frequently before the onset of indicative symptoms. However, such design of an effective population screening method requires very careful consideration (Cucchetti, Cescon, Erroi, & Pinna, 2013). Time consuming methods that require the use of expensive equipment and/or processes, run the risk of becoming economically unviable to be carried out on large volumes of patients. Low sensitivity methods leading to inconclusive results or misdiagnosis, requiring further medical investigation increases exposure to the risks associated with such procedures and will inevitably incur addition costs that would otherwise have been avoided.

Although NHS statistics highlight an increase in survival rates when compared to previous years, it is evident that there are still many cancers that are been diagnosed too late (Hawkes, 2019). Significant time-lags between diagnosis by screening and diagnosis through symptoms emphasises the need for more readily available screening technology, capable of detecting the earliest stages of cancer (Hatch et al., 2016). Widespread screening of high-risk populations has the potential to be a powerful lifesaving tool. However, careful considerations must be given to the possibility of exposing patients to the potential of harm that exceeds the potential benefit (Goodwin, Sheffield, Li, & Tan, 2016).

With high cancer survival rates been so often dependent on the early detection, molecular imaging presents a particularly useful approach in cancer screening. However, the current imaging technology required to carry out such detailed examinations often involves the use of harmful radiation and/or very expensive equipment. Therefore, the demand for a new non-invasive and inexpensive imaging modality that is safe enough to allow for more frequent screening to take place (both before and after cancer treatment) continues to be of great importance (Buccafusca, Proserpio, Tralongo, Rametta Giuliano, & Tralongo, 2019).

High frequency ultrasound is a non-invasive, non-ionising, portable and inexpensive imaging modality that has the potential to provide both functional and anatomical information in real-time. However, the only contrast agents currently approved and used in clinical molecular ultrasound imaging are microbubbles with diameters between 1-3 μm. Although these particles are often described as nanoparticles, their micron-scale diameters limit their ability to extravasate the blood pool into solid tumour masses and are therefore limited to only vasculature-based studies. The use of smaller contrast agent nanoparticles <100 nm diameter, have the potential to move US imaging from the restrictions of the blood pool into small tumour masses and therefore, enabling earlier detection of cancer. In addition to this, the smaller particles also have the ability to be retained within the area of interest long enough to be imaged without replenishment; something that microbubbles are currently unable to deliver on.

One of the major reasons why most of the newly developed nanosized contrast agents do not make it to clinical trials is the lack of in vivo quantification techniques available to fully assess the biocompatibility and toxicity of such nanoparticles in vivo. More research is needed towards developing a new imaging technology that is capable of quantifying nanosized particles in vivo, so that the in vivo behaviour can be fully characterised.

Therefore, this aspect of contrast enhanced imaging should be studied because doing so would drive development of new ultrasound imaging technology towards earlier detection and quantification of cancer.

1.2 Scope of the dissertation

The objectives of this work are to investigate the specific acoustic properties of a nan-sized material that can be used as contrast agents in clinical diagnostic imaging.

In order to achieve the objective, there are several limitations that need to be overcome. An imaging medium such as a tissue mimic will be developed with a well-defined particle size distribution to enable more accurate quantification of any acoustic response.

Chapter 2 reviews the background of currently available contrast enhanced imaging modalities and their ability to detect early stage cancer. Molecular imaging modalities that are not currently used in medical imaging are reviewed for their potential to translate into clinical applications. The current status of contrast enhanced ultrasound is reviewed, with focus on the use of NPs <300 nm as contrast agents for early cancer imaging diagnostics.

Chapter 3 describes the experimental set up and techniques used to prepare a monodispersed nanoparticle population of potential contrast agent <20 nm in diameter within a tissue mimic, and the ultrasound investigations that were undertaken.

Chapter 4 describes the results of preliminary investigations involving characterising the particle size distribution of the silica nanoparticles on diluting, heating and incorporating into the gelatine-based tissue mimic.

Chapter 5 describes the results of the ultrasound investigations carried out.

2: A review of contrast enhanced diagnostic imaging: current status and future prospects.

2.1 Introduction

In this chapter, a background of currently available diagnostic imaging modalities and their ability to detect early stages of cancer are discussed, with a view to better understanding the underlying principles that make these modalities a good diagnostic imaging tool. Future prospects for molecular imaging been translated to clinical practice are evaluated and the cost-effectiveness of each modality assessed. A brief overview of the many different contrast agents that are currently used in practice and those upcoming as the next generation of contrast agents are discussed, in addition to the more recent research efforts towards the use of nano sized particles as contrast agents in diagnostic imaging. The current status of contrast enhanced ultrasound imaging using high frequency ultrasound is reviewed and the major limitations that need to be overcome for this to be translated into clinical practice are identified. With this information in hand, an alternative approach to the more commonly used high frequency imaging systems that employ contrast agents >1 μm is suggested as the basis for this work.

2.2 Introduction to medical imaging

Medical imaging is a valuable diagnostic tool that enables anatomy and physiology to be visualized and studied for any irregularities or abnormalities that may be present in a patient's body. According to the diagnostic imaging dataset provided by the NHS statistical release in 2018, 42.7 million medical imaging tests were carried out in UK in 2018; of which, over a quarter of all tests requested by general practitioners was to diagnose or discount cancer (NHS, 2018). Medical imaging involves the passing an imaging probe such as x-ray or ultrasound through a patient's body to generate contrast data that can be exploited by an imaging modality to form images. The most commonly used imaging probes in clinical diagnostics include X-rays (radiography, CT, CR, DR, fluoroscopy and DSA), ultrasonic pressure waves (US), light (optical fluorescence imaging), nuclear medicine (PET and SPECT) and magnetic fields and radio waves (MRI, MRA, MRS and DTI). Although there are a growing number of medical imaging modalities that differ in their ability to provide detection sensitivity, spatial resolution, temporal resolution, signal-to-noise ratio (SNR), quantitative

accuracy and long term safety, none are capable of providing complete structural and functional information independently (Sharma et al., 2008). Therefore, selecting the right imaging modality that employs the most appropriate imaging probe depends strongly on the particular medical situation and disease to be studied (Wolbarst, Capasso, & Wyant, 2013). For high volume early cancer diagnostic screening, detection sensitivity and specificity towards the disease is key. However, the imaging capability required to detect small early tumour formation in vivo continues to be a great challenge.

In relatively recent years, molecular imaging has given birth to a wide range of imaging modalities that can be employed for the detection of early tumours. Molecular imaging is the in vivo visualisation, characterisation and quantification of biological processes at a cellular to molecular level. With a view to obtaining greater diagnostic accuracy and/or to enable greater imaging depths, the additional use of carefully designed contrast agents (CAs) has become a widely researched area, spanning across many disciplines. The development of such CAs that can help to visualise cancer proliferation and smaller tumour masses by exploiting the unique physical, chemical and biochemical properties thereof have enabled physicians to better study the indicative metabolic processes and characteristics of cancer microenvironments.

The correct selection of CAs for the imaging modality employed allows for CAs to significantly increase the degree of contrast, allowing for greater imaging depths and/or accuracy (Wu, Huang, Jiang, & Jiang, 2014). All modalities of contrast enhanced imaging require a contrast agent that is able to selectively identify the target tissue and accumulate within. However, the designing of a CA that is capable of specifically reaching the target cells and retaining there long enough to be detected presents a number of complex challenges (Chen & Chen, 2010). In addition to this, for imaging modalities with low sensitivity, the use of CAs with the multiple contrast functionalities may also be required if adequate levels of signal amplification are to be achieved (Debbage & Jaschke, 2008). The aim is therefore, to achieve the highest contrast as possible with high resolution and penetration depth for a minimal amount of contrast agent.

2.3 Comparing the most common imaging modalities used in cancer diagnostics

2.3.1 X-ray

Despite the discovery of X-ray imaging taking place over a century ago and well before the invention of advanced computing technology, radiography is still today the most frequently

used imaging modality for obtaining medical images world-wide (Wolbarst et al., 2013). With 22.9 million X-ray images and 5.51 million CT scans carried out in the UK in 2018, the use of electromagnetic waves in medical imaging and diagnostics continues to increase (NHS, 2018).

The most commonly used X-ray imaging modalities for the diagnosis of cancer are CT and mammographic imaging. Mammographic imaging is currently the most frequently used imaging modality for breast cancer screening (Miranda & Pertuz, 2019) and has also showed great potential in more recent years for breast cancer risk assessment (Gastounioti, Conant, & Kontos, 2016). However, mammography screening remains a very complex and relatively expensive imaging modality (Agide et al., 2018). In addition to this, mammography has in recent years received a number of criticisms for over diagnosis in women with dense breast tissue (Kuhl, 2018). Therefore, research efforts have now turned to alternative modalities for breast cancer screening modalities. In recently published article by Mori et al. (2018), MRI was shown to be powerful imaging tool in distinguishing between malignant and benign lesions, particularly in breast lesions.

CT plays a vital role in pathology diagnostics due to its ability to produce static 3-D visualisation of x-ray attenuation by tissues at an unlimited depth with exceptional spatial resolution (Liao et al., 2019). One of the biggest advantages of CT scan images over MRI is its high spatial resolution, which enables the visualisation of objects with poor contrast from within a patient. Offering a spatial resolution of up to 0.625 mm in the z-axis and 0.5 mm (approx.) in the x to y-axes, CT imaging offers spatial resolution up to the 1-2 mm typically associated with MRI (Lin & Alessio, 2009). Relatively recent developments in targeted high-performance CAs such as those described by Liao et al. (2019) shows a promising ability to provide greater contrast in CT images, with higher sensitivity. However, the contrast resolution provided with some MR modalities is still significantly superior to that of CT imaging.

The spatial resolution of CT images is largely dependent on the dose of X-ray administered. Higher doses result in higher signal to noise ratios therefore making it easier to visualise low contrast physiology (Goldman, 2007). With increasing concerns associated with the safety of radiation exposure in medical imaging (Mahesh & Morin, 2018), significant efforts have now turned to low-dose CT as a more promising screening modality (Bach, Brawley, & Silvestri, 2018; Smith et al., 2014). Recent developments in atomisation of lung cancer detection and characterisation (Kavitha, Shanthini, & Sabitha, 2019) in addition to advances in low dose CT technology, as reviewed by Callister and Janes (2017), makes for a convincing argument towards the use of low-dose CT in nationwide lung cancer screening. However, questions still remain concerning the implementation of widescale screening due to the expense of CT

imaging equipment, possibly rendering such screening economically unviable (Callister & Janes, 2017; Obaro, Burling, & Plumb, 2018).

2.3.2 Magnetic fields and radio waves

Whole body MRI modalities are now commonly used in full body examinations for early tumour detection (Pasoglou, Michoux, Larbi, Van Nieuwenhove, & Lecouvet, 2018). MRI is a nonionizing imaging modality that provides high-resolution 3-D anatomical images via the exploitation of hydrogen nuclei within a patient's body. By applying a strong magnetic field to the tissue of interest, the hydrogen nuclei within the tissue become uniform both in rotation and polarity. Once the uniform state has been established, short pulses of radio waves are passed through the tissue (the MRI sequence), causing the hydrogen nuclei to absorb energy and rotate out of equilibrium. After the radio wave transmission is eliminated, the nuclei are able to relax and energy is emitted (Schlemmer, 2009). Differences in the magnitude of energy released in addition to the time taken to return back to the original rotation is then visualised as contrast in diagnostic images, capable of superior soft tissue contrast to that of CT (Dommaschk et al., 2019).

Relatively recent MR modalities such as dynamic contrast enhanced MRI (DCE-MRI), arterial spin labelling (ASL), diffusion weighted imaging (DWI) and MR spectroscopic imaging (MRSI) are all able to deliver additional dynamic information in relation to the functional properties of malignant lesions (Schlemmer, 2009). This dynamic imaging modality is therefore providing valuable diagnostic information relating to the physiological status of pathology that is comparable to that provided in nuclear medicine (Wolbarst et al., 2013). In the recent work carried out by Morabito et al. (2019), DCE-MRI was demonstrated to be a good imaging modality for distinguishing between tumour reoccurrence and post-therapy necrosis. This type of capability in a diagnostic imaging modality would undoubtedly serve as a valuable tool in the monitoring of cancer progression, treatment planning and therapy. DCE-MRI is a real-time imaging modality which involves the administration of imaging CAs to enhance contrast and improve the quality of the resultant images. The additional benefit of DCE-MRI to static MRI imaging modalities is its ability to dynamically image vasculature. Because newly formed neovascular associated with cancer growth differs from the neovascular of normal tissues, this enables DCE-MRI to be used to further improve the detection of cancer (Du, Fu, Ren, Li, & Guo, 2019). In a sensitivity study carried out by Zhang, Zhang, Wang, Chen, and Sui (2019) of 47 articles reporting diagnostic data of liver metastases using DWI,MRI and CE-MRI, it was estimated that for liver metastases in lesions ≥ 10 nm in diameter, the sensitivity of DWI, MRI and CE-MRI were 93.1%, 92.9% and 94.5% respectively. However, the technology required

to produce such strong magnetic fields required for all MRI modalities, in comparison to other commonly used imaging modalities, remains very expensive. In addition to this, high doses of CAs are required to be administered, often with adverse effects.

MRI CAs are employed in CE-MRI for their ability to accelerate the relaxation times of the surrounding hydrogen nuclei, providing enhanced differentiation between surrounding tissues (Brown, Cheng, Haacke, Thompson, & Venkatesan, 2014). Among the most commonly used CAs in clinical applications of CE-MRI are gadolinium and iron oxide based particles (Na, Song, & Hyeon, 2009). Currently, the CAs used in CE-MRI clinical diagnosis are not sensitive enough to generate images with a high enough resolution to resolve a single cell; therefore limiting its application in very early disease assessments (Sharma et al., 2008). However, the development of a new generation of CAs have emerged in recent years exhibiting an increasing ability to accumulate in micro sized tumours with high levels of specificity. For example, in the work published by Du et al. (2019), a manganese-oxide mesoporous silica NP (85.4 ± 14.8 nm) was found to specifically target a rat prostate tumour within 5-10 nm of the malignant lesion.

When compared to CEUS imaging, DCE-MRI has been shown to have superior performance in the detection of prostate cancer and prediction of its aggressiveness (Baur et al., 2018). In a study carried out by Muhi et al. (2011) the diagnostic images of a solitary hepatic metastasis using CE-MRI, weighted MRI, DWI, B-mode US, CEUS and contrast enhanced CT (CE-CT) were compared for contrast and accuracy of diagnostic information. As shown in figure 1, the CE-MRI image obtained (a) via a gadolinium based CAs was able to provide an increased degree of contrast within the hepatic metastasis lesion (indicated by the arrow). When compared to the images produced via weighted MRI and DWI (b & c), these images gave less contrast and therefore less diagnostic accuracy than that of CE-MRI. However, in the images obtained using CE-CT (e) and B-mode and CEUS (d), the metastasis lesion was undetected. In great contrast to this however, a more recent investigation carried out by (Furrer et al., 2019) suggests that CEUS may be capable of outperforming CE-CT and CE-MRI for the diagnostic of renal masses. In this work Furrer et al. (2019) pooled together 1483 articles relating to the final diagnosis of benign and malignant renal masses for analysis. The results of this analysis suggest that CEUS gave a significantly higher level of sensitivity than CE-CT, reporting values of 0.96 (95% confidence interval 0.94-0.98) and 0.90 (95% confidence interval 0.86-0.93) respectively, and also a significantly higher sensitivity to that of CE-MRI, with values of 0.98 (95% confidence interval 0.94-1.0) and 0.78 (95% confidence interval 0.66-0.91) respectively.

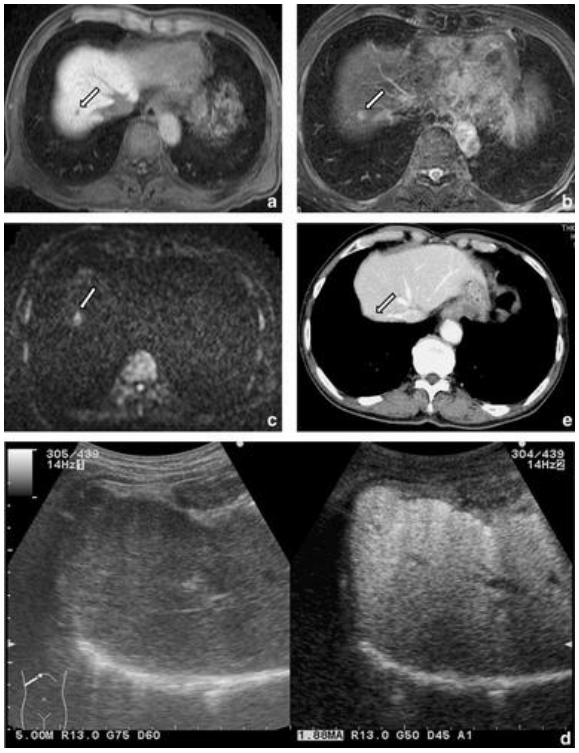

Figure 1. A pathologically confirmed hepatic metastasis (arrow) imaged using (a) Gd-EOB-MRI, (b) weighted MRI, (c) DWI, (d) B-mode US and CE-US, (e) CE-CT (Muhi et al., 2011).

2.3.3 Nuclear medicine

PET and SPECT imaging provides 3-D tomographic images via the use of tissue targeted carrier molecules containing radioisotopes. After the employed radioisotope tracers are administered to a patient, information depicting their location and concentration are processed to generate a 3-D visualisation of their distribution within a tissue of interest (Massoud & Gambhir, 2003). The active incorporation of radiotracers within bodily tissues therefore, unlike CT and MRI, offers the advantage of providing metabolic and functional information. The fundamental difference between PET and SPECT is that PET imaging modalities employ the use of positron emitting tracers whereas SPECT modalities differ in their employment of gamma-ray emitting tracers. SPECT carries a longer radiation exposure times than that of PET due to PET possessing higher energy and stronger photons, enabling a quicker exit from the body (LeVine, 2010). However, the correct selection of imaging modality to be used for a particular type of medical investigation depends essentially on the type of radiotracer that will deliver the most relevant diagnostic information.

The major purpose of PET scans is to detect and monitor cancer and tumours down to a cellular level. The direct targeting of cancer cells via glucose carrier molecules containing the employed tracer enables the rate of glucose metabolism within cancer cells to be visualised

using PET (Adekola, Rosen, & Shanmugam, 2012). This highly detailed metabolic information is a powerful tool in the monitoring of tumour progression and response to therapy. However, one major limitation of PET is that most anatomic structures in the images produced are either are poorly depicted or completely absent (Saif, Tzannou, Makrilia, & Syrigos, 2010). Therefore, most modern PET scanners also incorporate the use of CT to provide the additional anatomical information required for accurate diagnosis. Contrast enhanced CT imaging in addition to PET enables the better differentiation of the anatomical structures therefore, improved lesion localisation and characterisation can be made resulting in more accurate diagnostic information. In an article by Antoch, Freudenberg, Beyer, Bockisch, and Debatin (2004), CE-CT images were compared to that of PET, PET/CT and PET/CE-CT after a 47 year old female patient was administered with ^{18}F-FDG and CT contrast agent. As shown in figure 2, the hepatic metastasis of a 47 year old female patient was not distinguished in the CE-CT image (A). The PET image (B) shows increased glucose metabolism of the hepatic metastasis and therefore increased uptake of tracer however, very poor visibility of anatomical features was obtained. The combined PET/CE-CT image (C) visualises the accurately localised hepatic metastasis lesion and a biopsy device within viable tumour tissue (D) (Antoch et al., 2004).

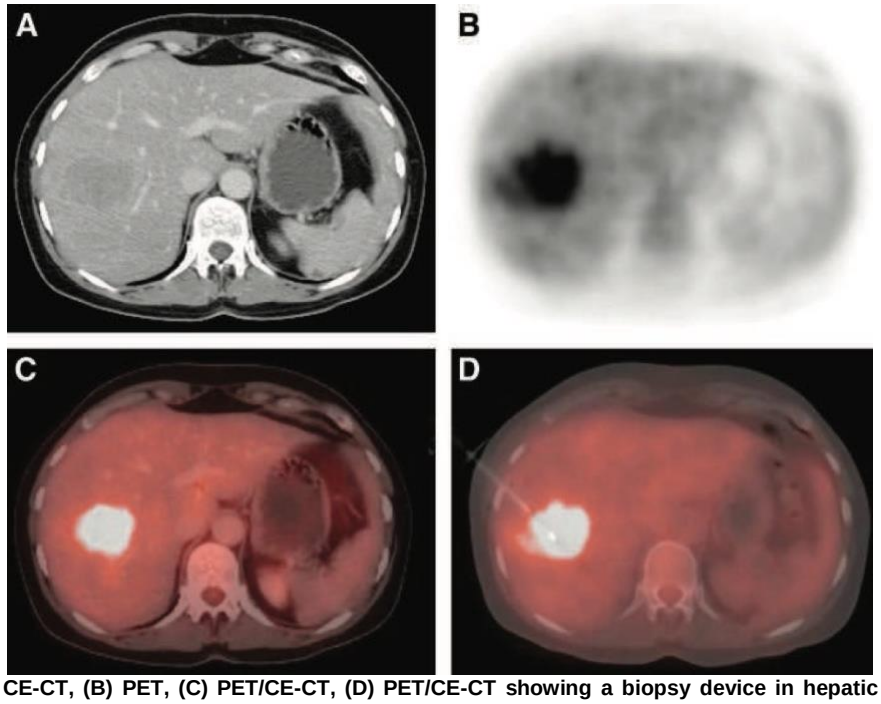

Figure 2. (A) CE-CT, (B) PET, (C) PET/CE-CT, (D) PET/CE-CT showing a biopsy device in hepatic metastasis lesion (Antoch et al., 2004).

Dual PET/CT modalities offers high diagnostic value in the diagnosis of many different types of cancer therefore, PET/CT is now the most common form of hybrid imaging used in clinical

diagnosis (Parisi et al., 2017). However, with both PET and CT involving exposing the patient to harmful radiation, efforts have now turned to lower dose PET/CT such as that described in the work by Molinos et al. (2019). As MRI offers as a non-ionising alternative to CT with comparable ability to determine local tumour extent, this type of multimodal PET/MRI approach contains a great degree of optimism for higher volume population screening. In the work carried out by Beiderwellen et al. (2015) it was found that both PET/CT and PET/MRI offer equivalently high diagnostic value in the diagnosis of recurrent pelvic malignancies. PET/MRI however, was found to offer a higher level of discrimination between benign and malignant lesions. In addition to this, Beiderwellen et al. (2014) found that whole-body MRI with PET/MRI also offered superior lesion visibility in bone metastasis images, with the added benefit of reduced radiation dose. Considering the reduced radiation dose superior lesion discrimination, PET/MRI offers the opportunity for a more desirable alternative multimodality.

Currently, PET is only diagnostic molecular imaging modality routinely used in medical diagnostics. Although PET/CT offers highly detailed metabolic information with high spatial resolution of anatomical features, PET is a static and very expensive imaging modality that uses highly ionising radiation. Therefore, PET is not a desirable choice for frequent post therapy monitoring or population screening (Conversano et al., 2011). Non-ionising alternatives to PET for early cancer detection is therefore of increasing importance. Such alternatives include optical imaging, dynamic CE-MRI and CEUS.

2.3.4 Optical imaging

Photoacoustic imaging (PAI) is a non-invasive, non-ionizing molecular imaging system that combines light with US to detect the consequential acoustic pulses arising from optical absorption. Visible light in the form of short laser pulses are used to induce transient heating within a patient's bodily tissues, causing a thermoelastic expansion of the tissue and subsequent generation of ultrasonic waves. The sound waves produced are detected by an US receiver and the data is exploited to produce high contrast images with high optical and spatial resolution, capable of providing structural, functional and biological information (Sharma et al., 2008). Recent developments in exogenous CAs exhibiting strong photothermal properties have been demonstrated to provide excellent contrast down to a molecular level. However, most of these particles are currently not permitted in clinical applications due to their cytotoxicity not yet been fully understood (Ho et al., 2014).

Optical imaging modalities typically achieve a spatial resolution of 1μm at 1mm depth however, unlike fluorescence tomography (FMT), the exploitation of the photoacoustic effect enables PAI to achieve deeper tissue imaging of up to 5cm deep (Borg & Rochford, 2018); With

comparable spatial resolution to that of US and still maintaining a high level of optical resolution (Dang et al., 2019; Ryu et al., 2013; Zhang et al., 2019). Although PAI has been shown to be an effective tool in molecular imaging at microscopic resolutions, unlike US, PAI application in deep tissue regions is limited by the attenuation characteristics of the light source (Witte, Karunakaran, Zuniga, Schmitz, & Arif, 2018). However, a recent comparison study between the different PAI imaging configurations currently available, carried out by Attia et al. (2019) reports that a penetration depth of up to 8.4 cm can be achieved in a chicken breast if the correct imaging configuration is employed.

PAI CAs are of particular interest in early cancer detection due to their small NP size, enabling them to accumulate in tumour tissue via the EPR effect. Gold nanoparticles (NPs) are one the most commonly researched PAI CAs due to its high photothermal conversion efficiency and biocompatibility (Sztandera, Gorzkiewicz, & Klajnert-Maculewicz, 2019). Photothermal conversion is the conversion of light energy (supplied by the PAI light source) to heat energy, inducing transient heating (X. Li et al., 2018). In addition to the strong photothermal properties of gold NPs, the negative surface charge also allows for surface functionalization and biomodification (McNamara & Tofail, 2016), allowing the NPs to be more easily modified to carry out a specific function. However, synthesis and functionalization of the gold nanorods still requires a number of challenges to be overcome. Concerns arise from the synthesis method which currently allows for large variations in particle size, and so significantly impacting yield (Shah, Imran, & Ullah, 2019). Therefore, the economic viability of producing precious metal NPs with low yield may limit the imaging system in its use as a high-volume population screening modality. In addition to this, the laser technology required to produce the sharp pulses of light capable of inducing deeper transient heating are generally very large and relatively expensive. However, in the paper written by Erfanzadeh and Zhu (2019) it was assessed that lower-cost light source alternatives can be explored. In addition to this, when compared to CE-MRI, MRI technology is significantly more expensive. Therefore, there continues to be an increase in demand for new nanoparticle technology that can further enhance the contrast obtained via PAI with a view to maintaining its characteristic high contrast and high resolution images at deeper penetration depths (Shah et al., 2019). This type of imaging technology would significantly enhance cancer detection by offering a non-invasive, non-ionising imaging system with the ability to detect small early cancer lesions via NP CAs.

2.3.4 Sound waves

Diagnostic ultrasound is a non-invasive, non-ionising imaging modality that employs sound waves to generate echo signal data that can be visualised as contrast between bodily tissues (sonograms). With most clinical frequency US scanners having the ability to image in a variety of different imaging modes, US can be readily used in the pre-diagnosis of a wide range of different diseases quickly, easily and using relatively inexpensive equipment (Mortimore & Mayes, 2019). However, the spatial resolution achieved using US is considerably less than that achieved by MRI and limitations in its use arise from sound wave inefficiency at passing across tissue/air or tissue/bone interfaces (Wolbarst et al., 2013); something an X-ray modality such as CT would deliver superior contrast in. In soft tissues however, low radiological differences between different soft tissues limits the contrast delivered using CT therefore, the contrast obtained using US is superior at imaging soft tissues than CT. Therefore, ultrasonography has advantages over CT in cost, lack of ionising radiation and improved spatial resolution however, CT images have superior diagnostic accuracy.

However, the interpretation of B-mode sonographic images is often described as been operator dependent. Correct identification and interpretation of differing features that can occur in a sonogram requires a great amount of skill and experience. In addition to this, these features can also vary significantly in sensitivity, specificity and positive and negative predictive values (Rowe, Osorio, Likhterov, & Urken, 2017). Therefore, the identification of sonographic features and interpretation thereof still lacks in an adequate degree of sensitivity and specificity to be able to independently diagnose or rule out malignancy (Lim, 2019; Melany & Chen, 2017). However, although B-mode imaging cannot be used to distinguish between malignant and benign tissue (Guo, Raghu, Durand, & Hooley, 2018), its ability to detect areas of interest for further investigation safely, quickly and cheaply still makes US a go-to choice in population screening (Kamal, Hamed, Mansour, Mounir, & Abdel Sallam, 2018; Ronot et al., 2018; Y. Wang et al., 2019). Therefore, the widespread use of sonography as a non-invasive, cost-effective high-volume screening tool for the monitoring and identification of pathological changes continues to be in great demand.

CEUS was first developed in the 1990's via the first generation of CAs consisting of non-enveloped air/oxygen echogenic microbubbles. In more recent years however, the most frequently utilised US CAs consist of phospholipid or protein stabilised hydrophobic gas core microbubbles (Song et al., 2018; L. Y. Wang & Zheng, 2019). When microbubbles are exposed to low amplitude US pulses, the microbubble is compressed and expanded with the positive and negative pressure phases of the pulse in an oscillatory fashion. At low acoustic pressures, the bubble response is linear, resulting in low echo signal gain and therefore low contrast. At increasing acoustic pressures however, the bubble response becomes increasingly non-

linear, resulting in an increasing degree of contrast that can be visualised. However, as the acoustic pressure is increased, the stability of the microbubble becomes increasingly compromised leading to bubble fission and eventually complete destruction of the microbubble (Mulvana et al., 2017).

Currently, there are two main types of CEUS imaging systems that are employed in clinical CEUS, single-pulse and multi-pulse imaging sequences. Each imaging systems has been designed to have increased sensitivity to specific microbubble behaviour. In single-pulse imaging, the microbubble is able to be distinguished from tissue based on the frequency content of the received echoes. The acoustic response of bodily tissue consists of a narrow range of scattered frequencies. However, the acoustic response of a microbubble is very broadband therefore, the received echo frequencies that are outside the range of the tissue echo can be selectively filtered to produce an image. The visualised contrast produced in the image will therefore correspond to the distribution and concentration of CA within the tissue and will only include minimal visualisation of tissue backscatter. This is the basis for harmonic (Menigot & Girault, 2016), super harmonic (Y. Li et al., 2016) and subharmonic imaging (Park, Kim, Cho, & Seo, 2016). Multi-pulse imaging sequences differ from single-pulse in that it exploits the different non-linear oscillations of a specific type of microbubble when exposed to a collection of US pulses with differing characteristics (Chong, Papadopoulou, & Dayton, 2018). Examples of multi-pulse imaging sequences include phase inversion and amplitude modulation (Satir & Degertekin, 2016). One major limiting factor for both single-pulse and multi-pulse imaging modalities however, is the poor signal-to-noise (SNR) ratio in deeper tissue regions. Due to the decreased SNR, a higher degree of bubble response is required to achieve the same degree of contrast. This increase in bubble response is achieved by increasing the acoustic pressure that is applied. However, increasing the acoustic pressure results in rapid decrease in signal duration due to bubble destruction therefore, the microbubbles will continuously need to be replenished. With the signal duration under typical imaging protocols currently standing below 5 minutes (Abenojar et al., 2019), the even more rapid signal decay under high acoustic pressures this limits the imaging time available for deeper tissue imaging. However, a new strategy recently proposed by Gong, Song, and Chen (2018) has suggested a way in which this particular challenge can be overcome. A combination of CEUS sequences with longer transmission pulses and multiplane-wave compounding method was used to improve the signal-to-noise (SNR) ratio in deeper tissues without increasing the acoustic pressure. In this work, it was found that the method employed had significantly improved the SNR of CEUS imaging without increasing the acoustic pressure. In addition to the imaging system design in CEUS, statistical systems such as the CEUS liver imaging reporting and data system proposed by (J. Li et al., 2019) have reported the ability to

improve the true-negative classification of HHC diagnosis. Such systems, in conjunction with more accurate imaging powered by CAs and system design are therefore showing exciting new ways in which cancer detection and diagnosis can be taken into high volume population screening (Bertolotto et al., 2018). However, although the clinical use of CEUS with microbubbles has increased considerably in the past 5 years, there are still many issues to be overcome regarding their in vivo stability and polydisperse size distribution. When a microbubble is exposed to an US pulse, bubble coalescence and gaseous core dissolution can occur. This results in reduced imaging time durations and half-life circulation time (Song et al., 2018). Stabilisation methods such as the lipid shell-stabilised perfluoro propane recently proposed by Abenojar et al. (2019) have been demonstrated to prolong in vivo stability however, many efforts have now turned to hard-shell microbubbles as an alternative method to improve in vivo stability of US CAs. The 'harder' the shell, the less sensitive the bubble becomes to US exposure at low acoustic pressures. However, hard shell microbubbles are more capable of withstanding higher acoustic pressures and therefore improving in vivo stability and SNR in deeper tissue. Another common problem associated with microbubble CAs is the polydisperse characteristics of those commercially available and approved; typically 1000-3000 nm in diameter (Gnyawali et al., 2017). As smaller microbubble sizes exhibit less echogenic behaviour, monodisperse microbubbles are more desirable than polydisperse characteristics (Pellow, Goertz, & Zheng, 2018). However, the synthesis of monodisperse microbubbles that have the circulation half-life times required for medical imaging continuous to be a challenge (Gnyawali et al., 2017).

Unlike the CAs used in CE-MRI and CE-CT, CEUS microbubbles are too large to extravasate the blood pool and enter the interstitial space of solid tumours (Chong et al., 2018). As newly developed vasculature of cancer lesions differs to that of normal tissue, vascularity studies using CEUS such as that carried out by Kummer et al. (2018) have shown to be a good indicator of cancer size and pathological severity. However, one major limitation of CEUS in molecular imaging is the lack of sub-micron sized US CAs that have the ability to extravasate out from the vasculature into the interstitial fluid (Lim, 2019; Zlitni & Gambhir, 2018). However, the synthesis/generation of stabilised, monodispersed microbubbles with strong echogenic properties and long lifetimes is very technically challenging (Perera et al., 2017; Son, Min, You, Kim, & Kwon, 2014).

2.4 Contrast targeting strategies

CAs used in diagnostics can be either exogenous or endogenous. Many of the CAs that have been employed in clinical imaging consist of soft shell nanoparticles such as the gas filled

microbubbles for CEUS, hard shell particles and particles that incorporate signal generators such as iron oxide, gadolinium, fluorine, iodine, bismuth, radionucleotides, quantum dots, and metal nano-clusters (Debbage & Jaschke, 2008). The specific targeting of CAs to malignant tissue is area of research that has expanded rapidly in the past 20 years, resulting in many new CA designs emerging with unique physiochemical properties such as size, shape and surface chemistry (Barua, 2018; Ruoslahti, 2012; Shobaki, Sato, & Harashima, 2018; Wilhelm et al., 2016). However, the efficiency of a CA reaching a target lesion such as a solid tumour continues to be a great challenge. A comprehensive analysis carried out by Wilhelm et al. (2016) of nanoparticle delivery efficiency to tumours over a 10 year period between 2005-2015 found that only a median of 0.7% of the administered dose of NP was able to reach a solid tumour. NP less than 5nm in hydrodynamic diameter were found to be excreted by the renal clearance pathway and NP >5nm taken up by phagocytic cells of the mononuclear phagocytic system (MPS), eliminating 99% of the injected dose. However, NP with hydrodynamic diameters <100nm were found to have a higher delivery efficiency than NP >100nm. In addition to this, NP with neutral zeta potentials (defined as -10 to +10 mV) were also found to have a greater delivery efficiency than those with negative (<10mV) and positive (>10mV) zeta potentials. Active targeting strategies such as the use of NPs with functionalised ligands complementary to the target sites were found give greater delivery efficiencies than passive targeting strategies such as enhanced permeability and retention effect (EPR), and rod shaped NPs exhibited higher efficiencies than spherical, plate and other shapes (Wilhelm et al., 2016).

Preclinical research, as discussed in Sulheim et al. (2018), has demonstrated that NPs and macromolecules have the ability to accumulate in solid tumours due to the EPR effect. However, the EPR effect is still been disputed by many as an effective targeting strategy. The EPR effect is a passive tumour targeting strategy which allows nano-sized particles and molecules to accumulate within tumour tissue to a greater extent than in that of normal tissues. When tumour cells multiply to reach a cluster size of 2-3 mm, the growth factor for the formation of new blood vessels (angiogenesis) is triggered to meet the new oxygen and nutrition demands of the growing tumour mass. The newly formed neovascular differs from the neovascular of normal tissues in that it is irregular in shape, dilated, reduced (or absent) smooth muscle layer and possess defective endothelial cells that are poorly aligned or disorganised with large fenestrations (Iyer, Khaled, Fang, & Maeda, 2006). These anatomical defects allow for excessive leaking of blood plasma components (such as contrast probe NPs) into the tumour tissue. Furthermore, tumour tissue experience poor lymphatic clearance and reduced venous return and so the extravasated plasma components are retained for a prolonged period of time resulting in particle retention (Conversano et al., 2011). Very high

local concentrations of NPs smaller than a pore size of tumour endothelium (typically 380-780nm) are able to temporarily reside within the tumour tissue (Conversano et al., 2011; Iyer et al., 2006). However, NPs with diameters less than 10 nm are also able to extravasate from normal capillaries therefore, the use of NPs is limited to >10 nm in order to discriminate between normal and leaky capillaries (Wilhelm et al., 2016) and allow for the passive infiltration of tumours without infiltrating the surrounding normal tissues (Pellow et al., 2018).

Although active targeting strategies have been shown in many investigations to be the most efficient method of delivery (Wilhelm et al., 2016), these investigations mostly compare this strategy to studies of non-targeted particles with diameters >380 nm. As decreasing particle diameter increases extravasation, NP CAs with diameters <100 nm are more likely to be dominated by the EPR effect (Vallet-Regi, Colilla, Izquierdo-Barba, & Manzano, 2017). Therefore, smaller NP sizes would result in less non-specific retention, giving a greater differentiation between malignant and benign tissue.

Poorly targeted CAs in vivo can dramatically reduce the degree of contrast obtained in all imaging modalities. High level background noise caused by CAs with non-specific retention can overwhelm the signal gain and essentially drown it out. For high signal to noise ratios to be achievable therefore, relatively large volumes of CAs are required to build up in within or around the specific site of interest for the images produced to be diagnostically accurate. Molecular imaging NPs that are small enough to extravasate into blood capillaries and come equipped with surface functionalisation to improve stability and biocompatibility, as well as target specific cells within the body are now emerging as the next generation of NPs (Chong et al., 2018; Feinstein et al., 2010; Marcelo, Lodeiro, Capelo, Lorenzo, & Oliveira, 2020; Martinez et al., 2010; Vallet-Regi et al., 2017). These NPs have already shown great promise in their application of early disease detection however, complete studies that consider the biodegradability, biocompatibility and toxicological effects of such NPs are particularly rare. Therefore, the field still lacks in sufficient understanding of in vivo NP behaviour (Marcelo et al., 2020). More contrast agent specific imaging technology that has the capability to image such NPs with high resolution is therefore of great importance if in vivo detailed assessments of the toxicology, biocompatibility, biodegradability and accuracy to be carried out.

2.6 High frequency CEUS imaging

Although non-targeted microbubbles are been used increasingly in clinical US molecular imaging, BR55 is currently the first and only clinical grade molecularly targeted US CA that has been FDA-approved (Abou-Elkacem, Bachawal, & Willmann, 2015; Willmann et al., 2017). The BR55 microbubble consists of a gas core of N_2 and C_4F_{10} stabilised by a phospholipid shell that is functionalised with a heterodimer peptide specific for VEGFR2 (Smeenge et al., 2017). BR55 has been successfully applied in a first safety and feasibility study for prostate cancer detection and VEGFR2 expression in breast and ovarian lesions (Abou-Elkacem et al., 2015; Willmann et al., 2017). However, due to the diameter of the BR55 CA and other FDA-approved non-targeted microbubbles (typically 1-4μm dia.), these US CAs are limited to only vasculature based studies such as; inflammation imaging, inflammatory bowel disease, inflammation in atherosclerosis and oncological imaging (Abou-Elkacem et al., 2015). In addition to this, there are still many issues to be overcome regarding microbubble in vivo stability and polydisperse size distribution. Therefore, many efforts have now turned to hard-shell microbubbles as an alternative method to improve in vivo stability and give better control over particle size distribution.

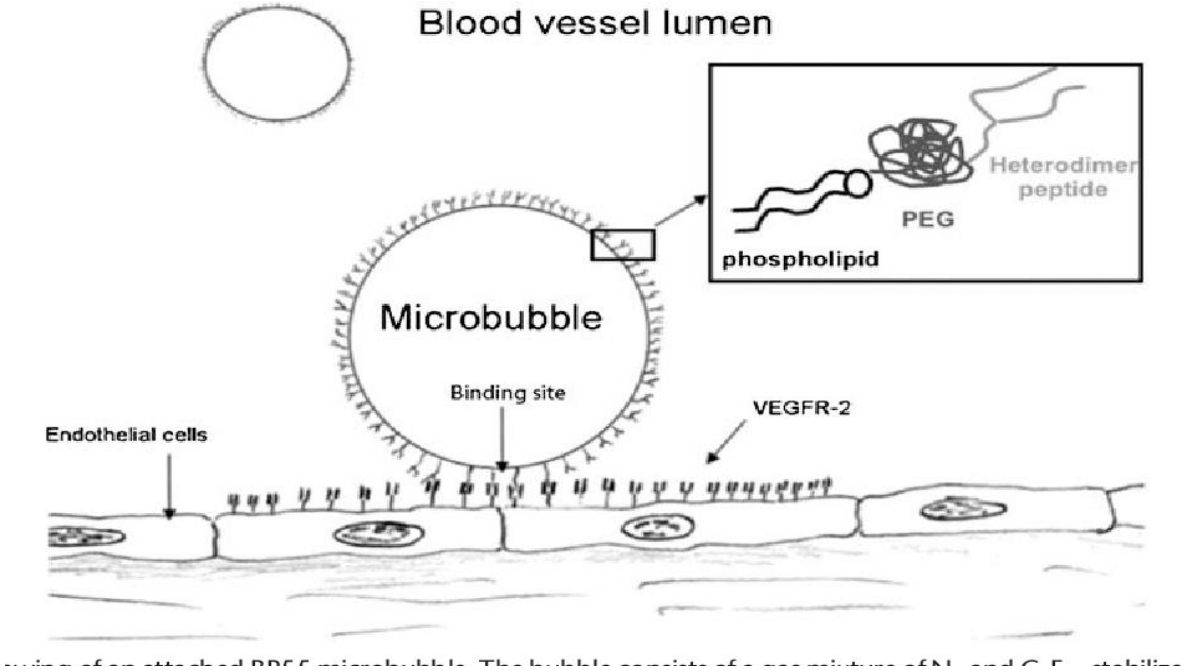

Figure 3. A schematic of an attached BR55 microbubble (Smeenge et al., 2017).

The most frequently used hard shell microbubbles consist of biodegradable polymers and silica (Song et al., 2018). The most commonly researched hard-shell NP material used in US imaging is silica (SiO_2). Silica has been used in a wide range of biomedical applications due

to its unique properties including controllable particle size, good biocompatibility and biodegradability (Marcelo et al., 2020). Nano-porous silica shells are advantageous due to their smaller uniform sizes and low toxicity (Martinez et al., 2010). Mesoporous silica in particular has gained an increasing amount of attention in more recent years due to its high surface area to volume ratio that can be exploited by surface functionalisation and theragnostic applications (Vallet-Regi et al., 2017).

Hollow nanoparticles made from silica and polymer shells exhibit good echogenic properties by their ability to expand and contract under low acoustic pressures without coalescence or destruction (De Jong, Bouakaz, & Frinking, 2000). However, unlike echogenic soft shell microbubbles, harder shell microbubbles and NPs exhibit significantly lower echogenic properties therefore, the contrast obtained by such hard shell microbubbles and NPs is still highly dependent on concentration (Song et al., 2018).

The imaging contrast obtained via hard shell particles with little echogenic response is obtained through differences in attenuation between the particles and surrounding tissue. The greater the concentration of CA within the area of interest, the greater the degree of attenuation and therefore the greater degree of contrast gained in the images produced. Attenuation by absorption occurs when a particle oscillates under acoustic pressure. The differences in density between a NP and its medium causes motion of the particle with respect to the medium and shear wave friction is induced, resulting in losses of acoustic energy (Dukhin & Goetz, 2010). In grey scale imaging algorithms, the more highly absorbing regions will translate into less received signal compared to surrounding tissues therefore, areas of high CA populations will appear to be darker than those of surrounding tissue. In contrast to absorption, attenuation by scattering involves the redirection of acoustic energy rather than loss. The redirection of acoustic energy allows for the reflection to be received by a transducer as a signal gain. The signal gain is therefore translated as contrast by providing brighter shades of grey in grey scale algorithms. When a hard-shell particle is exposed to an acoustic pulse, attenuation due to absorption and scattering are distinctly separated in the frequency domain. For fixed particle sizes, absorption will dominate at low frequencies and scattering at high frequencies. For particles < 1 μm, scattering is insignificant at frequencies < 100 MHz. Therefore, for particles < 3 μm, losses in acoustic energy (attenuation) is dominated by absorption with negligible acoustic losses occurring from scattering with particles < 1 μm (Dukhin & Goetz, 2010). Therefore, particles within the size range of 1-3 μm fall within the transition stage between the two mechanisms resulting in both absorption and scattering occurring simultaneously. The consequence of this is that signal gain from scattering would be cancelled out by signal losses due to absorption and very little contrast would be observed.

However, for particle sizes < 1 μm or > 3 μm, the degree of contrast obtained will be largely dependent on the local concentration of particles within the area of interest. Although, for particle sizes < 1 μm, the high frequency US pulses required would also be highly attenuated by other structures within the biological tissue and significantly decreases the resolution at greater imaging depths. However, US attenuation is function of both depth and material therefore, by investigating the specific acoustic behaviour of a specific material of NP (< 1 μm), signal processing can be employed to narrow the frequency range employed to that at which the specific material of NP shows the highest degree of attenuation contrast with surrounding tissue. In contrast to the multi modal US scanners commonly placed in clinical settings, this type of US imaging modality will therefore be one that has a narrower range of application. However, as a non-invasive, non-ionising, inexpensive imaging modality with the potential to provide both functional and anatomical information in real-time, this particular type of imaging system shows immense promise. Therefore, the use of hard-shell NPs as US contrast agents with diameters < 100 nm and > 10 nm (the size of a healthy blood capillary pore) are a less researched but attractive choice of contrast agent for high frequency US imaging.

2.7 Summary

When applied to early cancer detection, molecular imaging can be used to both detect and locate tumour masses as well as provide the specific metabolic information required to assess the state of progression and/or response to therapy (Chong et al., 2018). With PET/CT and PET/MRI been the only molecular imaging modalities that are currently available in clinical practice, high frequency US imaging presents its self as a promising alternative imaging modality with the potential to provide both functional and anatomical information in real-time. High frequency US is a non-invasive, non-ionising, portable and inexpensive imaging modality that can be used in conjunction with small diameter silica NPs (10-100 nm) to move US imaging from the restrictions of the blood pool into small tumour masses. By investigating the acoustic properties of silica NPs with monodisperse particle size distributions, the specific relationship between the attenuation of silica at high frequencies can be deduced. This information will enable more specific signal processing and therefore increase the diagnostic accuracy and NP quantifying ability of the resultant imaging system.

Chapter 3: Experimental set up and design

3.1 Introduction

In order to investigate the specific acoustic properties of Silica NPs a broadband range of frequencies are required. A high frequency broadband transducer (centre frequency 50 MHz) will experience return signal losses due to absorption attenuation of the silica NPs under investigation. The signal loss in the time domain can then be transformed into the frequency domain using the Fourier transform for the silica NP attenuation to be calculated. Data spanning across a range of frequencies as provided by the broadband transducer can be used for further data analysis to investigate the acoustic relationship between the silica NPs and employed acoustic energy.

In order to accurately investigate the degree of attenuation caused by a monodispersed size range of silica NPs between 10-20 nm in diameter, the size distribution of the NPs employed in the US investigation must first be characterised. The use of tissue mimicking mediums are commonly used in US investigations to more accurately model the acoustic environment in which the NPs are held. However, in order for this method to be used, the particle size distribution of the silica NPs within the tissue mimic also requires characterisation. Dynamic light scattering instrumentation provides data for particle size distribution and zeta potential of colloidal dispersants (NPs). The data provided can be used to evaluate the particle size distribution and mean average particle size of the silica NP within the gelatine tissue mimic. However, as the principle of the measurements are based on Brownian motion, any testing of the NP/gelatine solution before it has solidified.

Small angle X-ray scattering is an analytical technique that measures the intensity of scattered x-rays as a function of scattering angle. When a sample is placed in front of an x-ray beam, the incident x-rays are scattered by the particles at characteristic angles. The scattered x-rays are detected and the angle at which the incident x-ray beam has been scattered is used to characterise the sample using a number of different data processing methods. The information provided will be indicative of the size, structure and surface properties of NP within the sample. This technique can therefore be used to support the data provided by the dynamic light scattering instrumentation.

Commercially available LUDOX colloidal silica is supplied in relatively high concentrations compared to those that are required in this investigation therefore, the commercially available 30.7 vol% colloidal silica must first be diluted before it can be used within the tissue mimics

for the US investigation. Ensuring that the stability of a colloidal system after a dilution has not been compromised, dynamic light scattering investigations can be used to identify any changes in particle size (indicative of aggregation) and zeta potential (indicative of the electrophoretically mobile particles). As before, small angle x-ray measurements can also provide information relating to the particle size of the dispersant as well as support the dynamic light scattering measurements.

3.2 Materials used

- LUDOX® HS-40 colloidal silica (SiO_2), 40 wt.% in H_2O, supplied by Sigma-Aldrich (product number 420816).
- Dr.Oetker powdered gelatine batch number 2-82-033056
- Borokapillaren 2.0 mm borosilicate glass mark tubes (80 mm length) supplied by Capillary Tube Suppliers UK
- Vegetable oil spray - Sainsburys
- BRAND macro 2.5 mL UV-cuvettes, Cat. No. 7591 70

3.1 Equipment used

- Malvern Instruments Limited, Malvern zetasizer model ZEN3600, serial no. MAL1053758
- Bruker small angle x-ray scattering instrument
- Jenway 3510 pH meter model 3510, serial no. 61512
- Brookfield viscometer model RVDV-II+, serial no. RT58636
- Tektronix DPO 7254 Digital phosphor oscilloscope – Supplied by the National Physical Laboratory, Tedington
- Olympus 5073PR pulse/receiver - Supplied by the National Physical Laboratory, Tedington
- Zeal spirit in glass thermometer series IP-39C-SIMILAR, serial no. 1848220 - Supplied by the National Physical Laboratory, Tedington
- Olympus Panametrics-NDTV358 50 MHz/0.25″ transducer, serial no. 855206 (transducer) - Supplied by the National Physical Laboratory, Tedington
- Olympus Panametrics-NDTV358 50 MHz/0.25″ transducer, serial no. 852201 (receiver) - Supplied by the National Physical Laboratory, Tedington

- Ultrasound measurements tank as provided by the National Physical Laboratory, Teddington UK

3.4 Experiments performed

3.4.1 Method 1: Staged dilution of 30.7 vol% colloidal SiO_2 to 1 vol% with H_2O (pH ~10)

30.7 vol% colloidal SiO_2 was diluted to a concentration of 1 vol% in 1 vol% stages until a final concentration of 1 vol% was achieved. Samples were taken at each stage of dilution and were placed into a zetasizer instrument to obtain zeta potential and particle size distribution data. The Malvern zetasizer software measurement settings were pre-defined via a standard operating procedure. The measurement settings that were defined are:

- Measurement temperature: 25°C
- Temperature equilibration time: 120 seconds
- Dispersant refractive index: 1.33
- Dispersant viscosity: 0.8872 cP
- Particle refractive index: 1.590
- Particle absorption: 0.01

Zetasizer measurements were taken using a 2.5 mL sample placed into a 2.5 mL disposable UV-cuvette. Zeta potential measurements were taken via the Malvern universal dip cell provided with the instrumentation.

1) 45 mL of 30.7 vol% colloidal SiO_2 was drawn from its storage container using a glass volumetric pipette and placed into a 200 mL glass beaker. The beaker was placed into an ultrasonic bath to be sonicated for 20 minutes before a 2.5 mL sample was taken. The sample taken was immediately placed into the zetasizer instrument to measure the zeta potential and particle size distribution of the 30.7 vol% colloidal SiO_2. The temperature, viscosity and pH of the liquid remaining in the beaker was recorded.

2) The first dilution stage was to dilute the original 30.7 vol% colloidal SiO_2 to 30 vol% using 0.99 mL of H_2O. The pH of the deionised H_2O that was used to dilute the colloidal silica was measured and adjusted using NaOH in order to match the pH of the colloidal SiO_2 to be within ±0.50 of the pH of the colloidal SiO_2. 0.99 mL of the pH adjusted H_2O was added to the 200 mL beaker containing the 45 mL colloidal SiO_2 dropwise in 0.1 mL droplets over 5 minutes. The solution was then left in the ultrasonic bath for a further 20 minutes. After 20 minutes of sonication, a 2.5 mL sample was taken and immediately placed into the zetasizer instrument

to measure the zeta potential and particle size distribution of the new concentration, 30 vol% colloidal SiO_2. The temperature, viscosity and pH of the liquid remaining in the beaker was recorded.

3) The second dilution stage was to dilute the 30 vol% colloidal SiO_2 to 29 vol% using 1.41 mL of the pH adjusted deionised H_2O used in stage 1. Like stage 1, the H_2O was added dropwise in 0.1 mL droplets over 5 minutes and left under sonication for 20 minutes before a 2.5 mL sample was taken. The sample taken was used to measure the zeta potential and particle size distribution of the solution made at 0 minutes out of the ultrasonic bath. The remaining 29 vol% solution was measured for temperature, viscosity and pH.

4) Subsequent dilution sages were carried out to dilute the SiO_2 concentration by a further 1 vol% in each stage. Each subsequent dilution stage was carried out in the same order as that described in the first and second stage of dilution. The amount of H_2O added at each stage was calculated as:

$$\frac{\text{volume of } SiO_2 \text{ remaining after smapling (mL)}}{\text{Desired concentration (vol\%)}} - \text{total volume remaining after sampling (mL)} \qquad (1)$$

For example, the volume of H_2O added for the first dilution was calculated to be:

$$H_2O \text{ required (mL)} = \frac{42.5 \times 0.307}{0.30} - 42.5 = 0.99 \text{ mL}$$

The 1 vol% staged dilutions were carried out until a final concentration of 1 vol% was achieved.

5) In addition to the zeta potential and particle size distribution measurements that were taken at 0 minutes out of the ultrasonic bath, measurements at 1 hr, 2 hrs, 24 hrs, 72 hrs and 7 days were taken for concentrations of 30.7, 25, 20, 15, 10, 5 and 1 vol% solutions.

3.4.2 Method 2: Dilution of 30.7 vol% colloidal SiO_2 to a series of concentrations with H_2O (pH ~10)

Deionised H_2O was used to dilute 30.7 vol% colloidal silica to a concentration of 1, 2, 3, 4, 5, 10, 15, 20 and 25 vol%. The pH of the deionised H_2O used was measured and adjusted using 0.1 M NaOH in order to match the pH of the colloidal SiO_2 to be within ±0.50 of the pH of the colloidal SiO_2.

For each desired concentration, the amount of H_2O (pH ~10) and stock colloidal SiO_2 (30.7 vol%) required was calculated by:

$$\text{Vol. of } H_2O \text{ required} - \text{Vol. of 30.7 vol\% } SiO_2 \text{ required} \quad (2)$$

$$\text{Vol. of 30.7 vol\% } SiO_2 \text{ required(mL)} = \frac{\text{required conc. (vol\%)}}{30.7 \text{ (vol\%)}} \times \text{required total vol. (mL)} \quad (3)$$

For example, the volume of stock 30.7 vol% colloidal SiO_2 required to make 200 mL of 1 vol% SiO_2 concentration was calculated to be:

$$\text{Vol. of 30.7 vol\% } SiO_2 \text{ required (mL)} = \frac{1}{30.7} \times 200 = 6.51 \text{ mL}$$

Zetasizer measurements were taken using a 2.5 mL sample placed in a 2.5 mL disposable UV-cuvette. Zeta potential measurements were taken via the Malvern universal dip cell provided with the instrumentation. The measurement settings were pre-defined via the software standard operating procedure defined in method 1 (section 3.4.1).

1) The required volume of H_2O (calculated by equations 2) + 2.5 mL was measured using a glass volumetric pipette and placed into a 200 mL beaker. The beaker containing the measured volume of H_2O was placed under sonication in an ultrasonic bath for 20 minutes before a 2.5 mL sample was taken. The sample (containing H_2O only) was placed inside the Malvern zetasizer for zeta potential and particle size measurements to be taken.

2) The required volume of the 30.7 vol% colloidal SiO_2 (calculated by equation 3) was added to the beaker containing the measured volume of pH adjusted H_2O in approximately 1 mL droplets over a time period of 5 minutes. The beaker contents were left under sonication for a further 20 minutes before it was lifted out of the bath and placed onto the work top.

3) The diluted colloidal silica liquid was measured for temperature, viscosity and pH. Samples of the liquid were taken at 0 minutes, 15 minutes, 30 minutes, 45 minutes, 2 hrs, 3 hrs, 24 hrs, 72 hrs and 7 days out of the ultrasonic bath and were placed into the Malvern zetasizer for zeta potential and particle size measurements to be taken.

3.4.3 Method 3: Dilution of 30.7 vol% colloidal SiO_2 to a series of concentrations with H_2O (pH ~7)

Deionised H_2O was used to dilute 30.7 vol% colloidal silica to a concentration of 1, 2, 3, 4, 5, 10, 15, 20 and 25 vol%. The pH of the deionised H_2O used was measured but was not adjusted to match the pH of the colloidal SiO_2 as per methods 1 and 2. The pH of the H_2O therefore was allowed to vary with the pH of the deionised H_2O supply to the laboratory. For each

desired concentration, the amount of H_2O (pH ~7) and stock colloidal SiO_2 (30.7 vol%) required was calculated by equations 2 and 3.

Each colloidal SiO_2 concentration was then prepared, sampled and measured using steps 1 to 3 as per method 2 (section 3.4.2).

Zetasizer measurements were taken using a 2.5 mL sample placed in a 2.5 mL disposable UV-cuvette. Zeta potential measurements were taken via the Malvern universal dip cell provided with the instrumentation. The measurement settings were pre-defined via the software standard operating procedure defined in Method 1 (section 3.4.1).

3.4.4 Method 4: Dilution of 30.7 vol% colloidal SiO_2 to a series of concentrations with H_2O (pH 5.0)

Deionised H_2O was used to dilute 30.7 vol% colloidal silica to a concentration of 1, 2, 3, 4, 8, 11, 15 and 20 vol%. The pH of the deionised H_2O used was measured and adjusted using 0.1 M HCl to pH 5.0. For each desired concentration, the amount of H_2O (pH 5.0) and stock colloidal SiO_2 (30.7 vol%) required was calculated by equations 2 and 3.

Each colloidal SiO_2 concentration was then prepared, sampled and measured using steps 1 to 3 as per Method 2 (section 3.4.2).

Zetasizer measurements were taken using a 2.5 mL sample placed in a 2.5 mL disposable UV-cuvette. Zeta potential measurements were taken via the Malvern universal dip cell provided with the instrumentation. The measurement settings were pre-defined via the software standard operating procedure defined in Method 1 (section 3.4.1).

3.4.5 Method 5: Dynamic light scattering of colloidal SiO_2 after heating to 55°C

Concentrations of 1, 2, 3, 4, 8, 11, 15 and 20 vol% colloidal SiO_2 solutions were prepared using a stock 30.7 vol% colloidal SiO_2 and deionised H_2O. The pH of the deionised H_2O used was measured and adjusted using a 0.1 M HCl to establish a H_2O pH 5.0. For each desired concentration, the amount of H_2O (pH 5.0) and stock colloidal SiO_2 (30.7 vol%) required was calculated by equations 2 and 3 (section 3.4.2).

1) The required volume of H_2O (calculated by equation 2) was measured using a glass volumetric pipette and placed into a 200 mL beaker. The beaker containing the measured volume of H_2O was placed under sonication in an ultrasonic bath for 20 minutes.

2) The required volume of the 30.7 vol% colloidal SiO_2 (calculated by equation 3) was added to the beaker containing the measured volume of H_2O (pH 5.0) in approximately 1 mL droplets over a time period of 5 minutes. The beaker contents were left under sonication for a further 20 minutes before it was lifted out of the bath and placed onto the work top.

3) Measurements of temperature, viscosity and pH were taken at room temperature at 0 minutes out of the ultrasonic bath.

4) The beaker and its contents were placed onto a hot plate with magnetic stirrer and were heated to 55°C. Measurements of temperature, viscosity and pH were taken at 55°C. A 2.5 mL sample was taken and placed inside the zetasizer instrument. Measurements of zeta potential and particle size distribution were recorded using the zetasizer equipment and software. The zetasizer measurements were carried out at 55°C with an equilibration time of 120 seconds, as pre-defined using a standard operating procedure within the zetasizer software.

5) The solution was allowed to cool to 25°C and measurements of viscosity, pH, zeta potential and particle size distribution were taken using the zetasizer instrument.

3.5.6 Method 6: Small angle x-ray (SAX) measurements of colloidal SiO_2 and SiO_2 in 8 wt.% gelatine

1) Sample preparation. Colloidal SiO_2 at concentrations of 1, 2, 3, 4, 8, 11,15 and 20 vol% were prepared as described in Method 4 (section 3.4.4).

2) Using a glass pipette, approximately 0.5 mL of the H_2O used to prepare the samples via method 4 was each loaded into a 2.0 mm borosilicate glass capillary tube as shown in Figure 4. The capillary tube was then sealed using bee's wax that was melted into the opening of the capillary to form a seal, as shown in Figure 4.

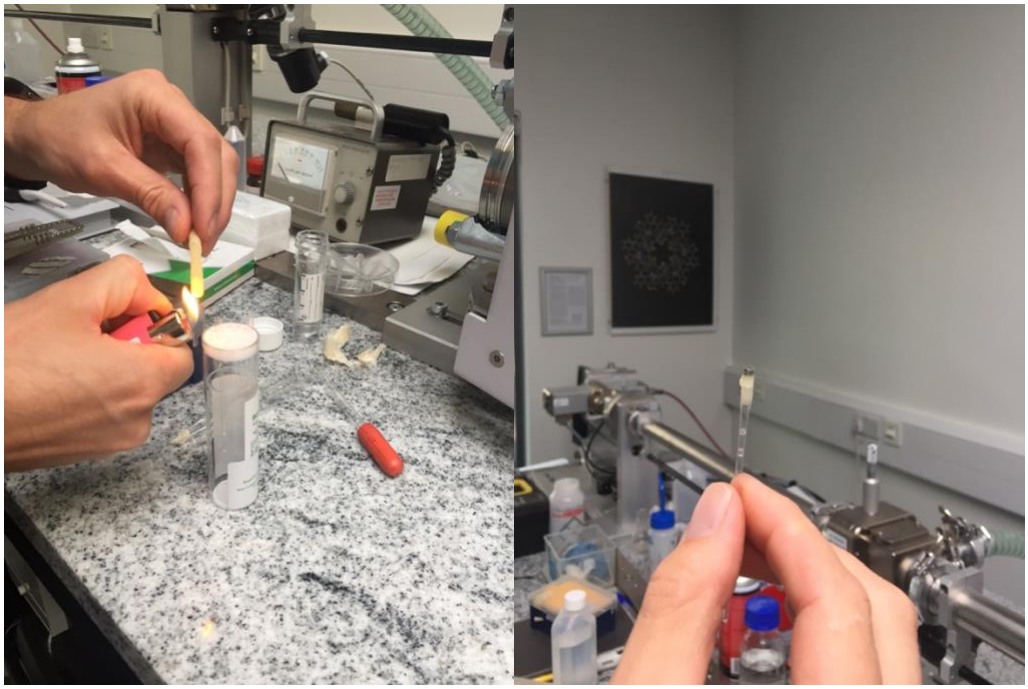

Figure 4: Bee's wax, melted and decanted into the opening of a 2.0 mm borosilicate glass capillary tube containing H_2O.

3) Due to the high fail rate of the fragile capillaries when put under vacuum a second capillary containing the H_2O used to prepare the samples was sealed via a second method. To seal the second capillary, the tube opening was held above a flame for approximately 5-10 seconds until the borosilicate glass at the end of the capillary had melted inwards and formed a seal.

4) The sealed capillaries were placed onto a mount and secured in place with screws as shown in Figure 5.

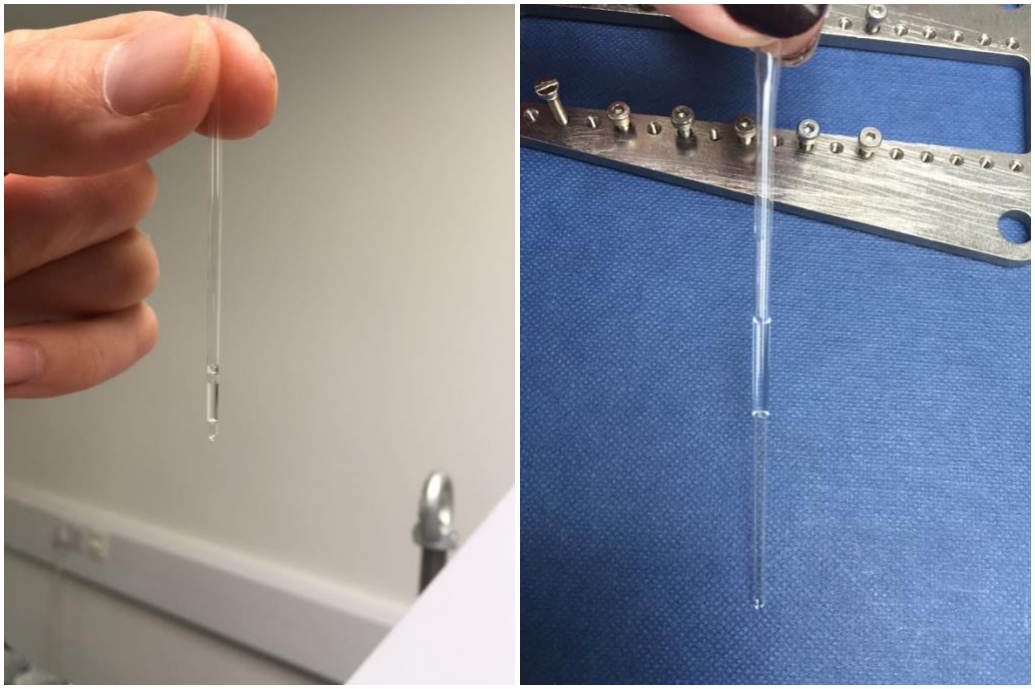

Figure 5: Borosilicate glass capillary containing H_2O (left), BRUKER small ang x-ray instrument sample mount (right).

5) The sample mount was placed within the vacuum chamber of the SAX instrument for data acquisition. An initial nomography was taken to locate the sample capillaries within the chamber as shown in figure 6. Once the capillary of interest had been located, the centre point of the sample was then located by determining the lowest point of intensity on the nomography, shown as the darker red regions in Figure 6. The X and Y coordinates of the centre of the sample was recorded and used as the co-ordinates for data acquisition.

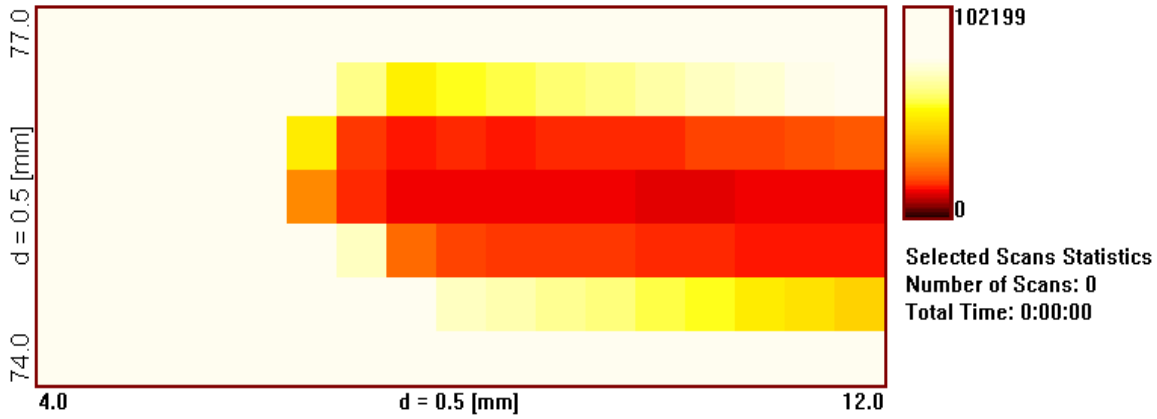

Figure 6: Small angle X-ray instrument nomography locating a 2.0 mm borosilicate glass capillary.

6) The measurement setting for the data acquisition were predefined using the SAX software as:

Distance: 107.650

Number of frames: 10

Seconds per frame: 600 seconds

7) The data acquisition as described in steps 1 – 6 was repeated for each concentration of colloidal SiO_2, 1, 2, 3, 4, 8, 11, 15 and 20 vol%.

8) The data acquisition as described in steps 1-6 was repeated for a 4 wt.% gelatine solution and an 8 wt.% gelatine solution containing a 1, 2, 3, 4, 8, 11, 15 and 20 vol% concentration of SiO_2.

3.4.7 Method 7: Preparation of 8 wt.% gelatine-based tissue mimics containing SiO_2

1) Colloidal SiO_2 at concentrations of 1, 2, 3, 4, 8, 11,15 and 20 vol% were prepared as described in Method 4 (section 3.4.4).

2) 62.5 mL of deionised H_2O was measured using a glass pipette and placed into a 150 mL beaker. The beaker was placed onto a hot plate with magnetic stirrer and heated to between 65-70°C. Once the temperature was reached, 7g of gelatine crystals were added and the hot plate was turned off. The beaker was held on the hot plate with the magnetic stirrer operating until the gelatine crystals were dissolved.

3) Once the gelatine solution was transparent to the eye, indicating that the gelatine crystals were dissolved, it was then carefully poured into a 10 cm diameter petri dish. Care was taken not to transfer any bubbles that had formed on the surface or any undissolved crystals that had stuck to the beaker walls.

4) 17.5 mL of the prepared colloidal SiO_2 concentration was injected into the solution using a 5 mL syringe. As shown on the left of Figure 7, the injected 4 vol% SiO_2 solution diffused into the gelatine solution on injection. The solution was agitated using the syringe needle to encourage mixing. Greater concentrations of colloidal SiO_2 were less diffusive than lower concentrations and so a greater amount of mixing was required. The image shown on the right of Figure 7 shows an 8 vol% SiO_2 solution been injected in the same manner as that shown in the 4 vol% on the left. However, bubbles were formed on mixing and the viscosity of the solution was notable increased. This change in viscosity was seen to an increasing degree

with increasing concentrations. As shown in figure 8, the highest concentration of SiO_2 (20 vol%) became very viscous compared to lower concentration and so a significant amount of air was trapped within the sample.

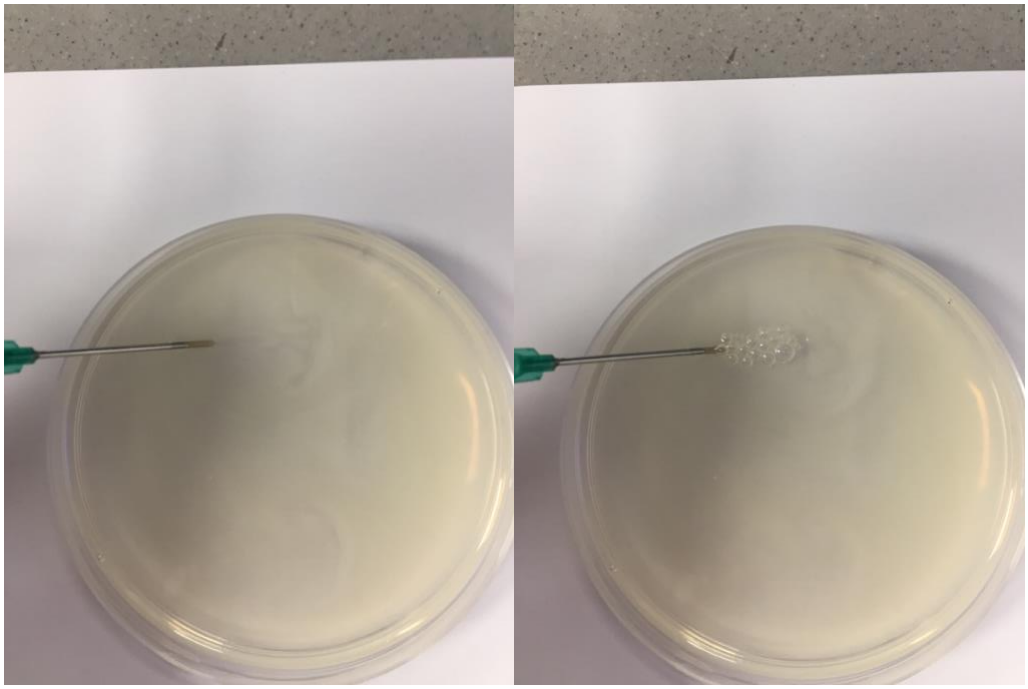

Figure 7: The visible diffusion of 4 vol% colloidal SiO_2 injected into 8 wt.% gelatine (left) and 8 vol% colloidal SiO_2 injected into 4 wt.% gelatine (right).

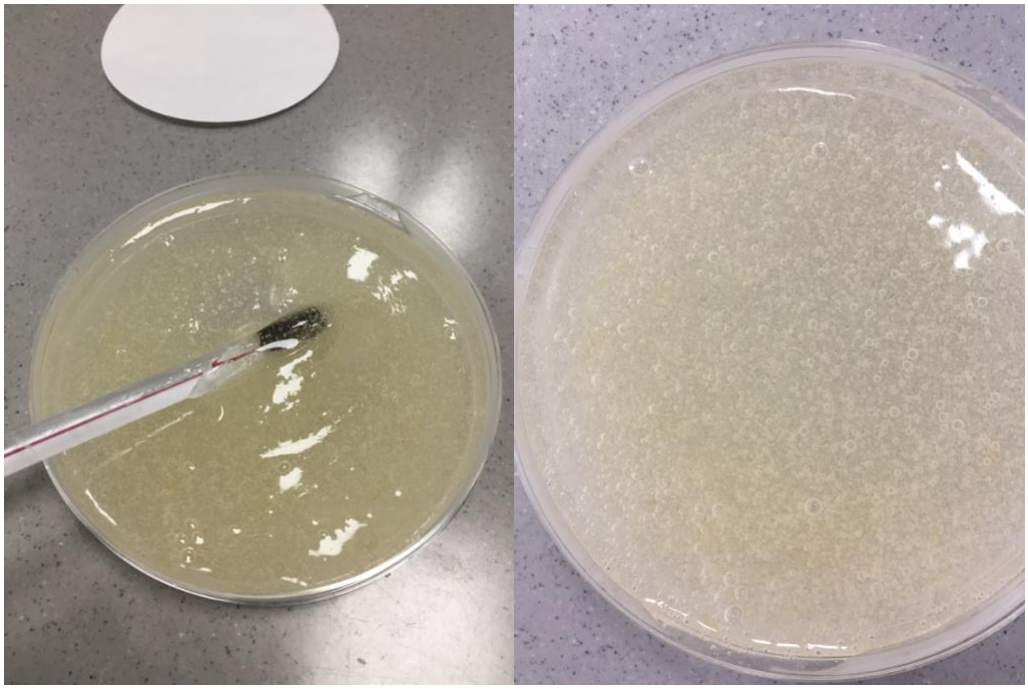

Figure 8: Bubbles trapped within the highly viscous 20 vol% colloidal SiO_2 and 8 wt.% gelatine solution.

5) The petri dish was placed into a preheated vacuum oven preheated at 50°C. The sample was held within the oven at 50°C under vacuum (~0.96 bar) for 1 hour. During this time, the bubbles trapped within the samples were drawn out. After 1 hour, the heat applied to the oven was turned off and the samples were left to cool under vacuum for another 1 hour.

6) The samples were removed from the vacuum oven and stored in a refrigerator at 3°C until required for further measurements (up to 12 hours).

3.5.8 Method 8: Dynamic light scattering measurements of colloidal SiO_2 in 8 wt.% gelatine.

1) Colloidal SiO_2 at concentrations of 1, 2, 3, 4, 8, 11,15 and 20 vol% were prepared as described in Method 4 (section 3.4.4).

2) 62.5 mL of deionised H_2O was measured using a glass pipette and placed into a 150 mL beaker. The beaker was placed onto a hot plate with magnetic stirrer and heated to between 65-70°C. Once the temperature was reached, 7g of gelatine crystals were added and the hot plate was turned off. The beaker was held on the hot plate with the magnetic stirrer operating until the gelatine crystals were dissolved.

4) The beaker was taken off the hot plate and 17.5 mL of the prepared colloidal SiO_2 concentration was injected into the solution using a 5 mL syringe. The solution was agitated using the syringe needle to encourage mixing.

5) The solution was allowed to cool to 25°C at room temperature before a 2.5 mL sample was taken. The sample was transferred into a 2.5 mL disposable cuvette and placed into a zetasizer instrument for zeta potential and particle size distribution measurements to be taken.

3.4.9 Method 9: Ultrasound attenuation measurements of gelatine-based tissue mimics containing SiO_2 NPs with a 50 MHz centre frequency broadband transducer

1) The US measurements tank was filled with de gassed water.

2) Two 50 MHz transducers were clamped into place using the measurements tank brackets as shown in Figure 9. The two faces of the transducers were held in place ~5mm apart, facing one another as shown in Figure 9. The transducer shown on the left of Figure 9 was employed

as a receiver in receive mode and the transducer shown on the right-hand side of Figure 9 was employed as the transducer to generate the US pulses.

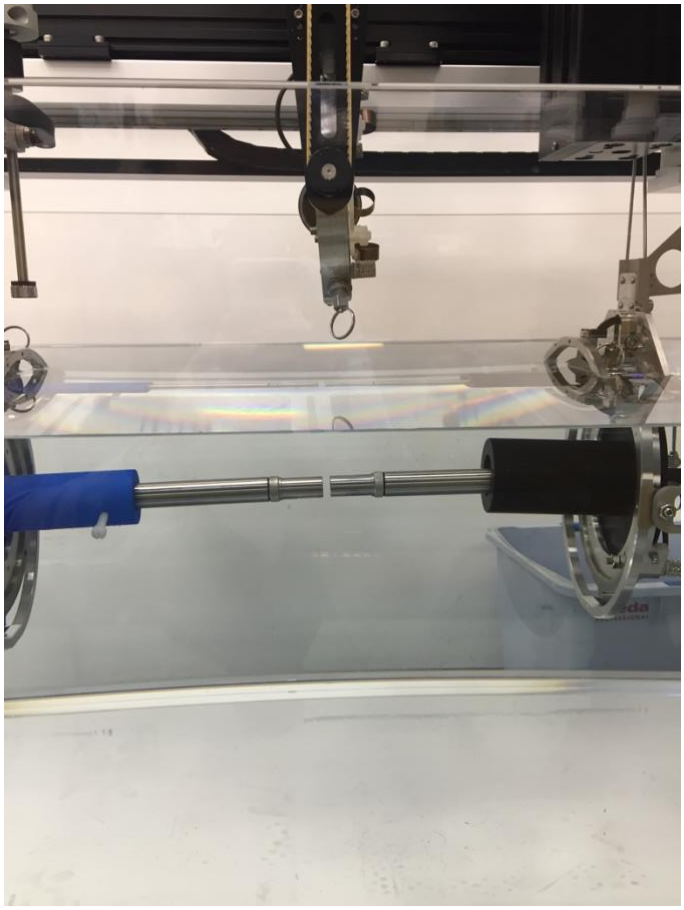

Figure 9: A 50 MHz transducer (right) and receiver (left) (picture taken at the ultrasound laboratory at the National Physical Laboratory, Teddington)

3) The experimental set up was allowed to stand for 1 hour after set up to allow for any background noise and/or bubbles within the tank to be dissipated.

4) To ensure that the transducer face was correctly aligned with the receiver, the receiver position was fixed in place and the power was switched on. The following power settings were set;

- Gain: +19
- PRF (Hz): 1K
- Energy: 4
- Damping: 8
- Mode 2 (isolates transmit and receive to give through transmission)

5) An alignment of the transducer face with the face of the receiver was carried out at minimum distance apart (horizontal delay 12.76 μs). The transducer face was translated in the X and Y axis in order to locate the centre of the receiver face. The centre point on the receiver face is the point at which the voltage received is at its maximum. As shown in Figure 10, the voltage peak shown on the oscilloscope before translation (left) gave a lower peak to that received after the receiver centre was located (right).

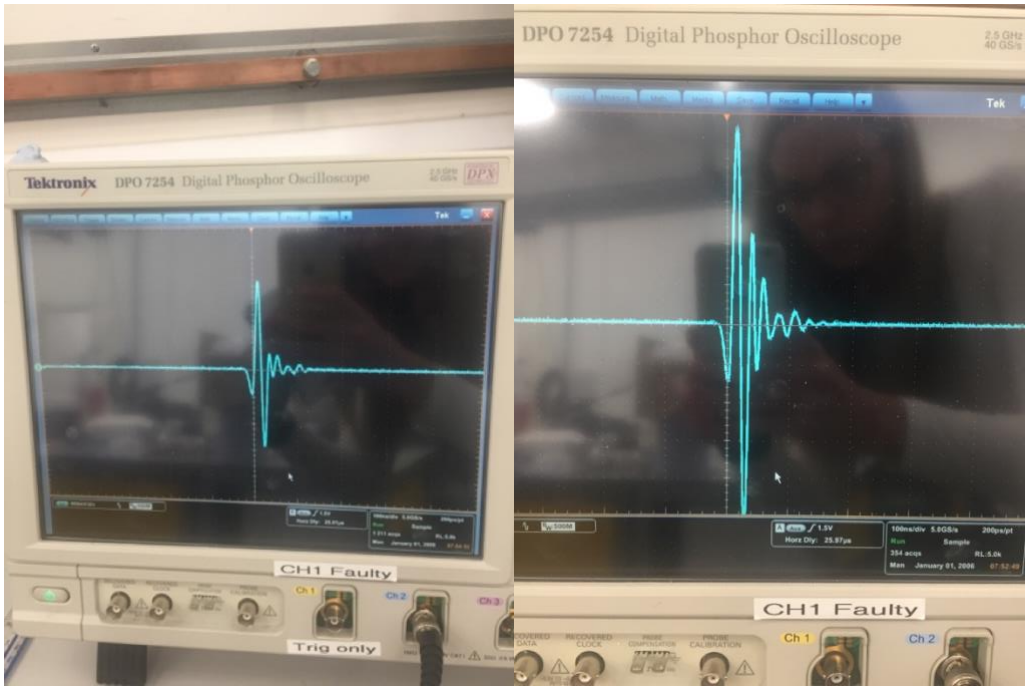

Figure 10: Wave form of the 50 MHz transducer before (left) and after (right) alignment with the centre of the receiver face. (picture taken at the ultrasound laboratory at the National Physical Laboratory, Teddington)

6) Once the centre of the receiver was located, the transducer face was aligned parallel to the receiver face by rotating transducer and receiver about their centre point. As in step 5, the point at which the two faces are parallel is the point at which the highest voltage can be received.

7) A second alignment of the transducer and receiver as described in steps 5 and 6 was carried out at maximum distance apart (horizontal delay 43.70 μs).

8) the thickness of each samples to be used in the US measurements was measured prior to been lowered into the measurement tank. The thickness measurements were taken at 4 separate points on the sample using a digital thickness gauge and the average was taken.

9) The first sample to be measured (gelatine reference sample) was secured onto the sample holder. The transducer was moved backwards, away from the receiver to allow space for the

sample to be placed in-between. As shown in Figures 11 and 12, once the sample was lowered, the transducer face was brought as close as possible to the sample holder without obstructing the holder from been lifted out of the water.

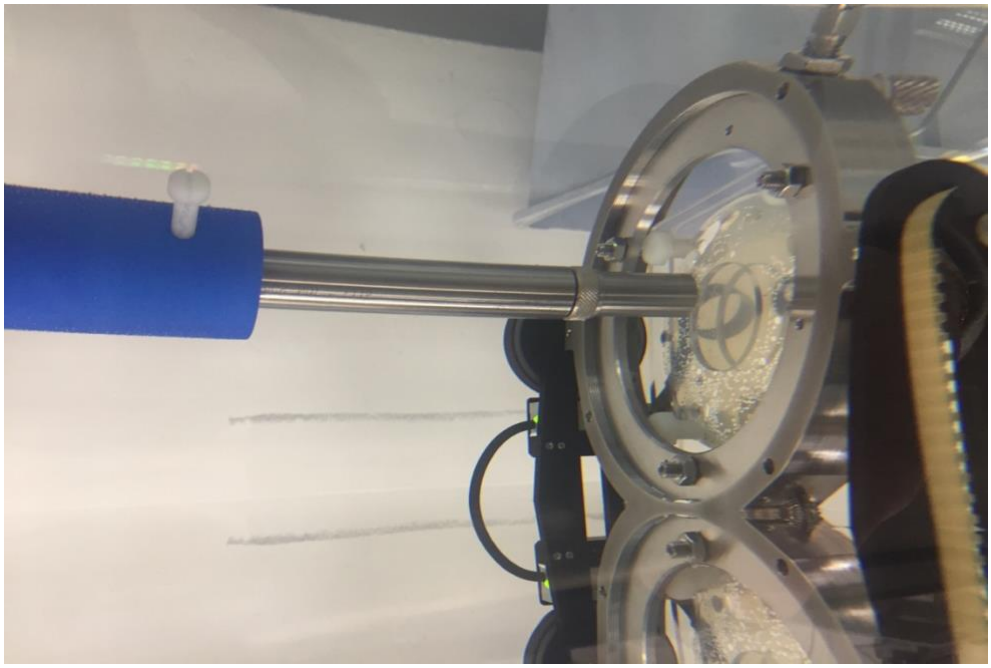

Figure 11: US receiver on left hand side of tissue mimic sample (picture taken at the ultrasound laboratory at the National Physical Laboratory, Teddington)

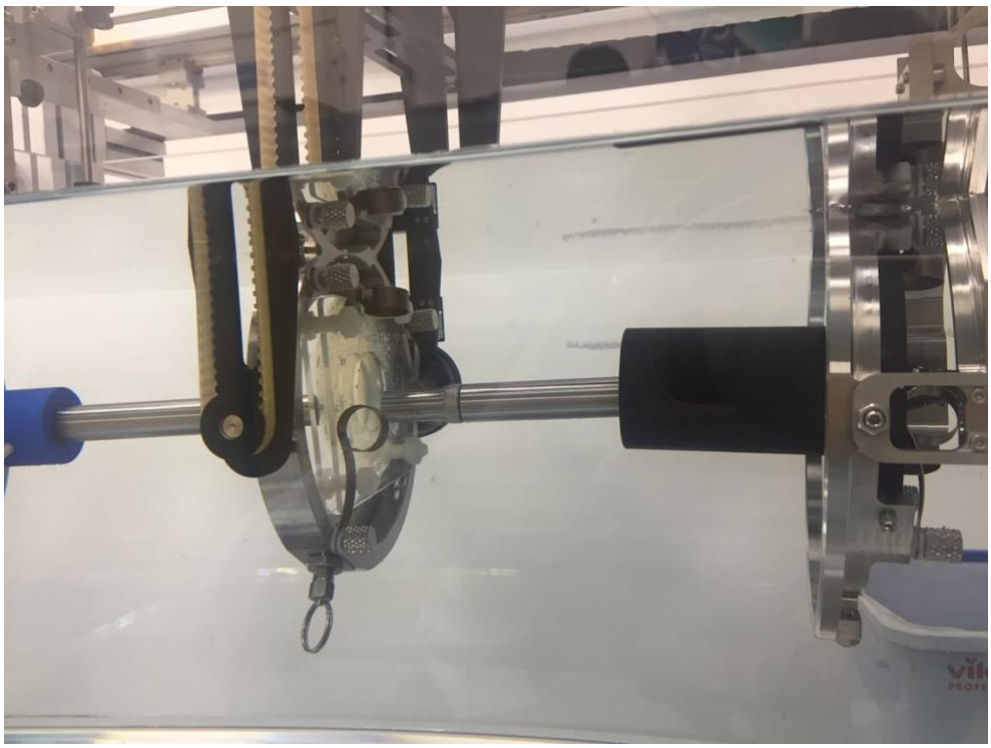

Figure 12: US transducer on right hand side of tissue mimic sample (picture taken at the ultrasound laboratory at the National Physical Laboratory, Teddington)

10) The energy setting was adjusted for data acquisition to;

- Gain: +25
- PRF (Hz): 1K
- Energy: 4
- Damping: 8
- Mode 2 (isolates transmit and receive to give through transmission)

10) For each sample, the following measurements were taken through the centre point of the sample, with 5000 scope averages;

- Reference transmission (without sample in place) at 26 μs horizontal delay
- Sample through transmission at 26 μs horizontal delay
- Reference transmission (without sample in place) at 27 μs horizontal delay
- Sample through transmission at 27 μs horizontal delay
- Reference transmission (without sample in place) at 28 μs horizontal delay
- Sample through transmission at 28 μs horizontal delay
- Reference transmission (without sample in place) at 29 μs horizontal delay
- Sample through transmission at 29 μs horizontal delay

11) For samples of 0, 1, 3 and 8 Vol%, grid measurements were taken 2 mm apart from one another in the -ve and +ve X and Y axis.

3.5 Summary

Investigations into the stability of the colloidal silica dilutions at each stage of the tissue mimic synthesis was investigated. Dilutions of colloidal silica were carried out via a number of different methods in order to investigate the effects of pH, temperature and viscosity on the colloidal system.

The pH of the colloidal silica (outsourced) used in the tissue mimic synthesis was pH 10 ±0.5. As the pH of gelatine is ~5.0, the effects of pH on the dilution of the original colloidal silica was investigated by altering the pH of the H_2O used in the dilutions to pH 10 ± 0.5, pH 5.0 and pH 7. Dynamic light scattering measurements were taken of each dilution with the different H_2O solvents so that the data could be used to identify any changes in the aggregation state due to the effects of varying pH.

To investigate the effects of heating the diluted colloidal silica during the tissue mimic synthesis, dynamic light scattering measurements were taken of the diluted colloidal silica after heating to 55°C and then after allowing this to cool back down to 25°C. The data provided was used to compare with the measurements taken at 25°C without heating to identify any changes in aggregation state induced by the heating process.

The PSD of the SiO_2 NPs within the tissue mimic after synthesis was measured in order to define the mean particle size of silica NP used in the US investigations. The data provided was used to compare with the data of the colloidal silica before the addition of gelatine to investigate the effect of the synthesis method on the PSD.

Small angle x-ray measurements were taken of the colloidal silica dilutions and gelatine containing SiO_2 NPs in order to support the data obtained from the zetasizer instrument.

US measurements were carried out using a broadband 50 MHz centre frequency transducer to investigate the attenuation of the silica NPs across a frequency range of 10-60 MHz. Each measurement was carried out with a reference measurement and at 4 separate horizontal delay distances to assure that the attenuation data collected was a direct function of the NPs present within the sample.

Chapter 4: Results and discussion of preliminary investigations carried out to define the size distribution of the nano-contrast agent.

4.1. Introduction

Before the contrast enhanced ultrasound measurements can be carried out the silica nanoparticles must first be prepared for imaging. Commercially available colloidal silica nanoparticles are available in significantly higher concentrations to that required in this work. Therefore, the colloidal silica was diluted to a range of concentrations that can be used in the synthesis of an acoustic tissue mimic. Tissue mimics are commonly used in research to model the behaviour of biological tissue. However, many for the publications that employ tissue mimics for contrast agent studies give little information on the particle size distribution of the particles therein. As the acoustic properties of nanoparticles can vary significantly with particle size, a full characterisation of the particle size distribution must first be carried out. With that information in hand, the acoustic investigations can be carried out under the assumption of monodisperse particles with a defined size distribution.

4.2. Results and discussion

The volumetric mean particle sizes measured using dynamic light scattering gave a mean particle size range of 5-20 nm. In the colloidal silica dilutions carried out via Method 1 and Method 2, the pH of the colloidal system was maintained by altering the pH of the deionised water used, to within ±0.5 of the colloidal silica. As changes in pH can lead to neutralisation of the surface charge of the silica NPs, the consequential decrease in electric repulsion, this allows for intermolecular interactions to dominate (Van der Waals) and aggregates are formed. However, as shown in Figures 13 and 14, the controlling of the pH in Methods 1 and 2, did not completely prevent aggregation therefore, the average particle diameter was found to increase in both methods as a function of decreasing concentration.

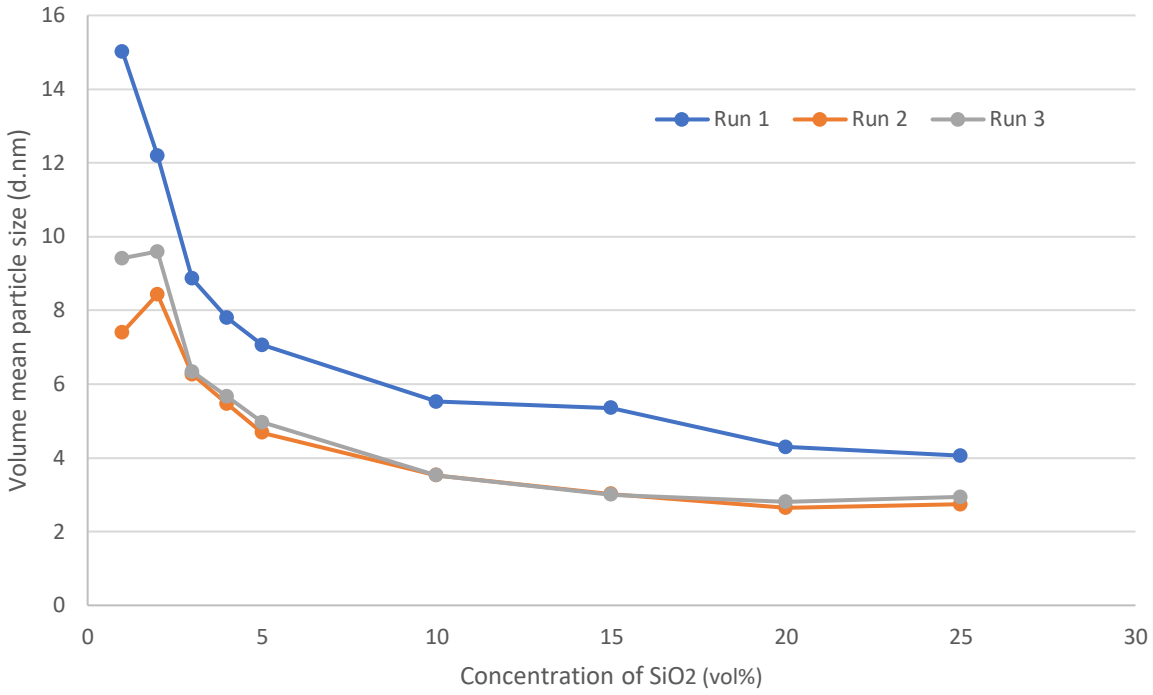

Figure 13: Increased mean particle size (d. nm) with decreasing concentration via Method 1.

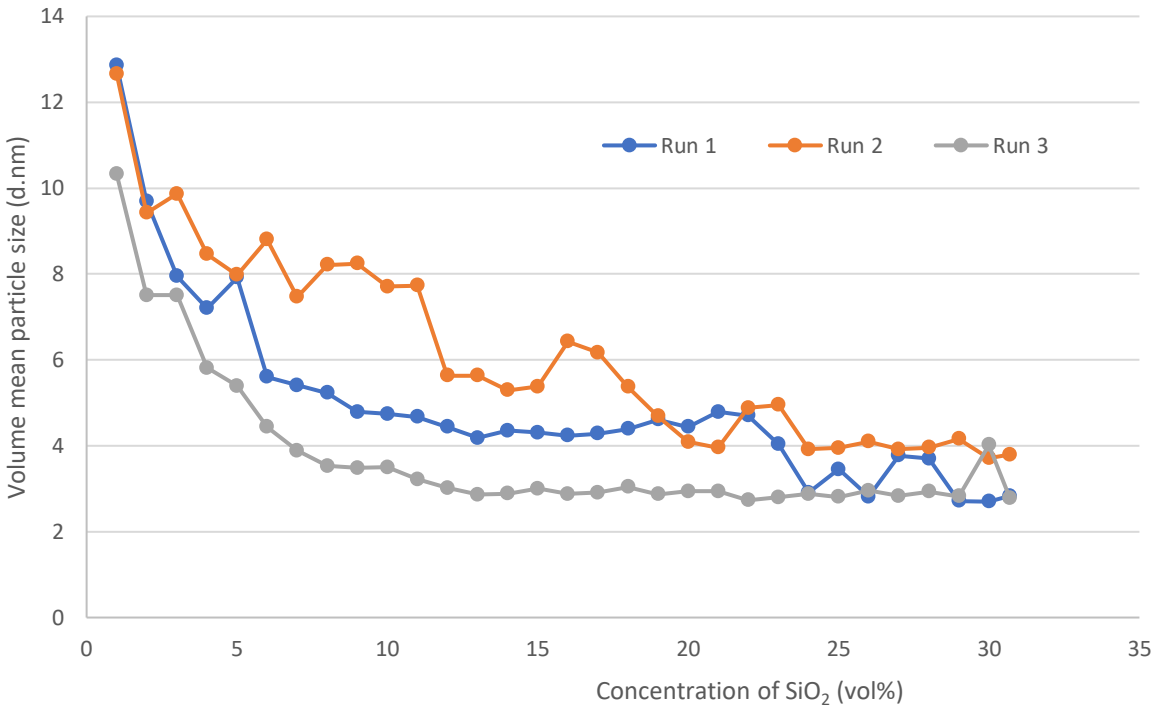

Figure 14: Increased volume mean particle size (d. nm) with decreasing concentration via Method 2.

The mean zeta potential of silica nanoparticles with unmodified surfaces in water increases with particle size (Metin, Baran, & Nguyen, 2012). Therefore according the data published by Metin et al. (2012) shown in Table 1, the LUDOX silica nanoparticles used in the dilutions of Methods 1 and 2 should carry a zeta potential between -48.7 mV to -79.8 mV depending the state of aggregation induced by the dilution.

Particle Diameter	Mean Zeta Potential
5 nm	-48.7 mV
25 nm	-60.3 mV
75 nm	-79.8 mV

Table 1: Mean Zeta Potentials for non-surface functionalised silica nanoparticles in water.

The zeta potential of each sample taken throughout the dilutions of Methods 1 and 2 are shown Figure 15 and 16 for methods 1 and 2 respectively. It can be seen that in both cases, the zeta potential of the colloidal silica became increasingly more negative as the dilutions were carried out. Although mean zeta potentials are a function of concentration, in this case the concentration is been reduced therefore, the increases in negative charge is primarily due to an increase in particle diameter, as shown in table 1.

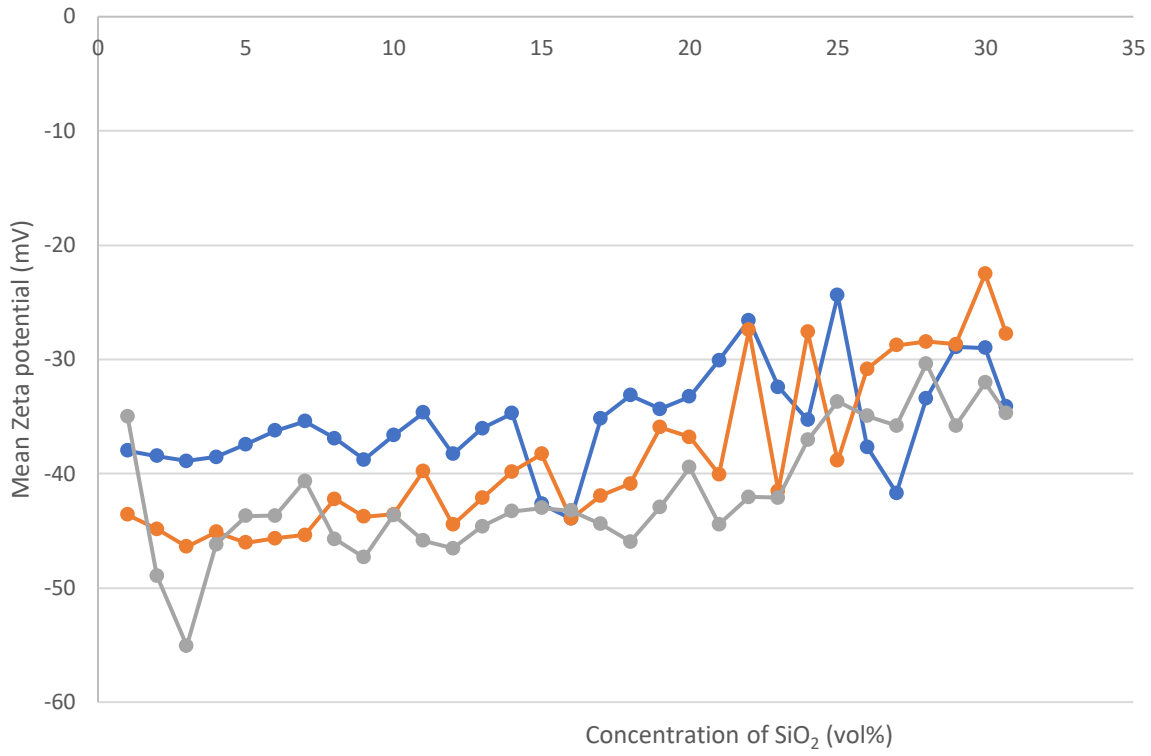

Figure 15: Increased negative mean zeta potential with decreasing concentration via Method 1.

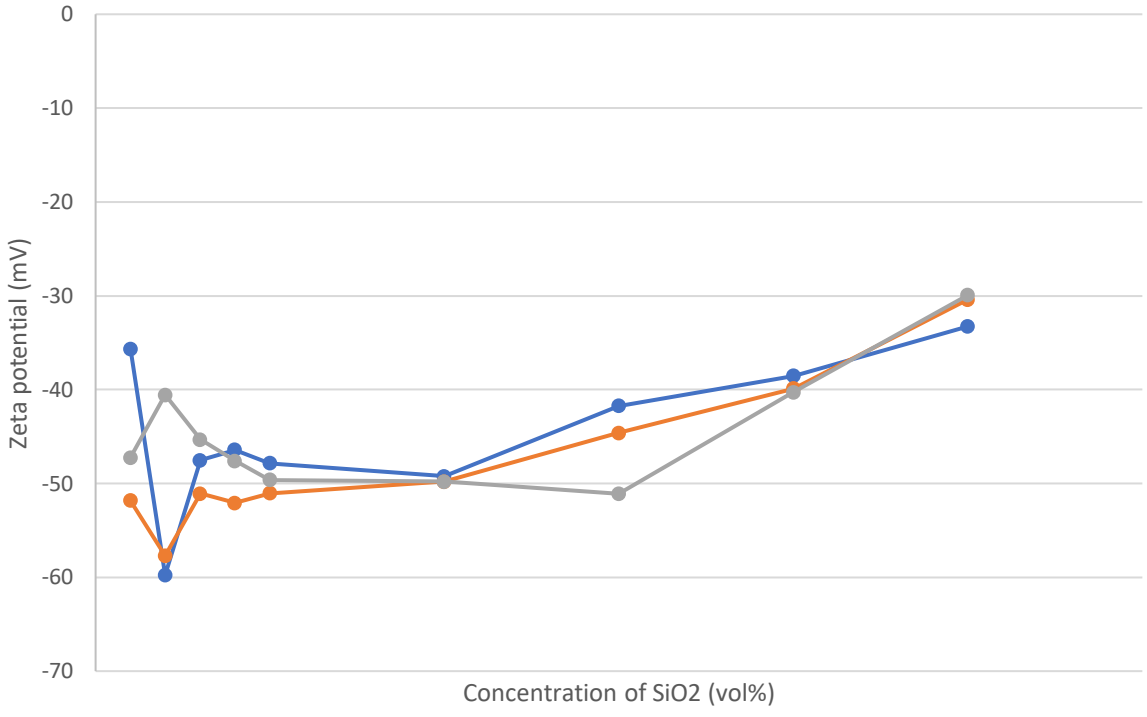

Figure 16: Increased negative mean zeta potential with decreasing concentration via Method 1.

In an article by T. Wang, Ni, Luo, Shou, and Cen (2012) it was noted that both size and pH can be found to significantly affect the viscosity of colloidal nanoparticle systems. The degree of aggregation caused by pH surface neutralisation and the shape in which the aggregates form are all contributing factor to increasing the viscosity of the system. However, the viscosity of the colloidal system diluted via Method 1 and 2 were in both found to decrease significantly with the relatively large quantities of water in which it was been mixed. Therefore, no increase in viscosity due to aggregation was observed. However, the rapidly decreasing viscosity of the system may have had an effect on the collision kinetics, resulting in aggregation. As shown in Figures 17 (Method 1) and 18 (Method 2), a strong trend can be observed between increases in particle size and decreases viscosity. This relationship seems to be more profound at very low centre poise viscosities, < 0.6 cP. This suggests that the less viscous nano-systems that were synthesised will exhibit a greater collision coefficient and therefore greater care must be given when introducing energy to the system in the tissue mimic synthesis method, Method 7.

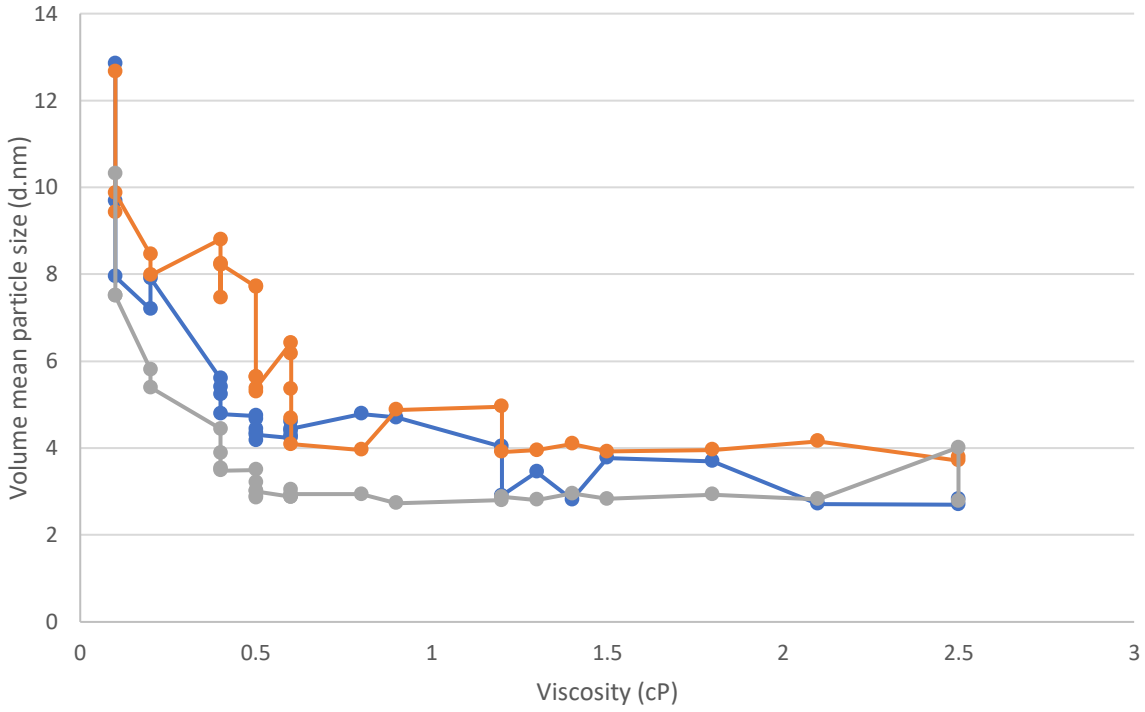

Figure 17: The relationship between viscosity and particle size as found during the investigations of Method 1.

Highly dispersed nanoparticles have a zeta potential greater than + 30 mV or less than – 30 mV (Abenojar et al., 2019). For nanoparticles within the +30 mV to -30 mV range, a lesser degree of electrostatic repulsion is experienced and therefore a greater probability of collision leading to aggregation. The system is therefore considered to be unstable.

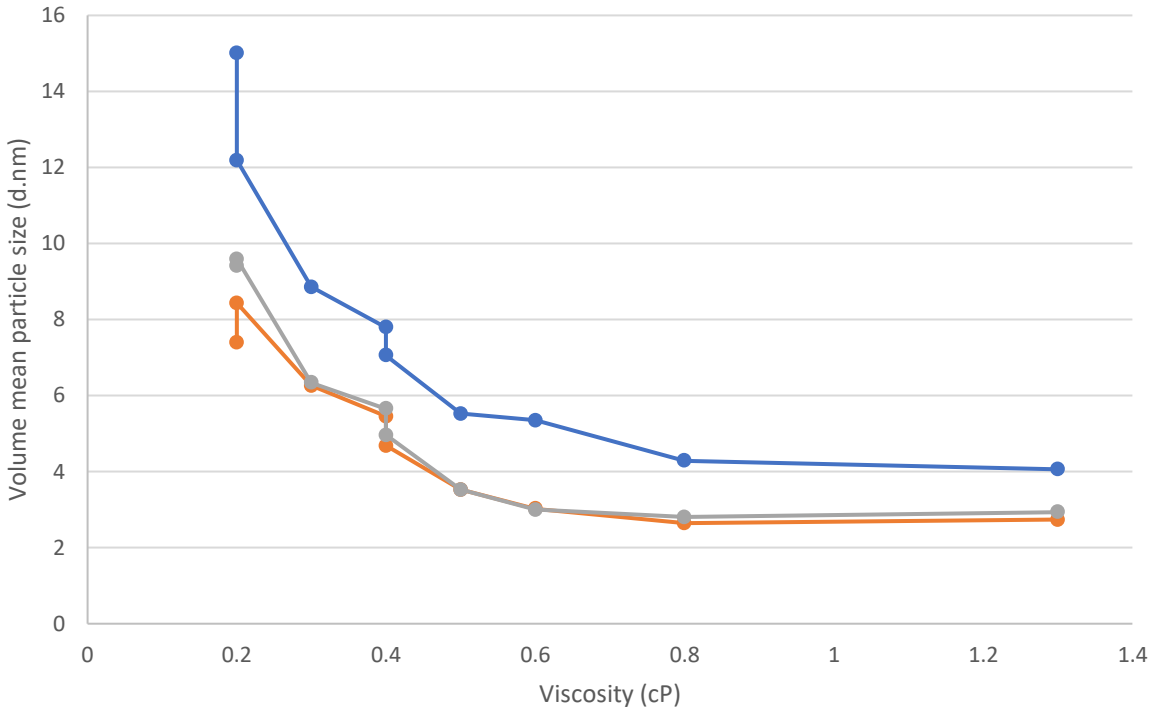

Figure 18: The relationship between viscosity and particle size as found during the investigations of Method 1.

Colloidal silica nanoparticles are stabilised by Si-OH salts therefore are basic in pH (~pH 10). Changes in pH, such as through the addition of gelatine (~pH 5) in Method 7 has the potential to neutralise the zeta potential of the colloidal silica and reduce its stability. The investigations carried out in Methods 2, 3 and 4 were to investigate the effects of inducing a more acidic environment on the stability of the colloidal silica. The measured mean zeta potentials of the colloidal silica that had been diluted using water of pH 10, pH 7 and pH 5 are shown in Figure 19. The measurements were repeated at regular intervals over 7 days. As shown in Figure 19, the mean zeta potential of the nano-system using pH 10 water was surprisingly less negative that those prepared using pH 7 and pH 5.

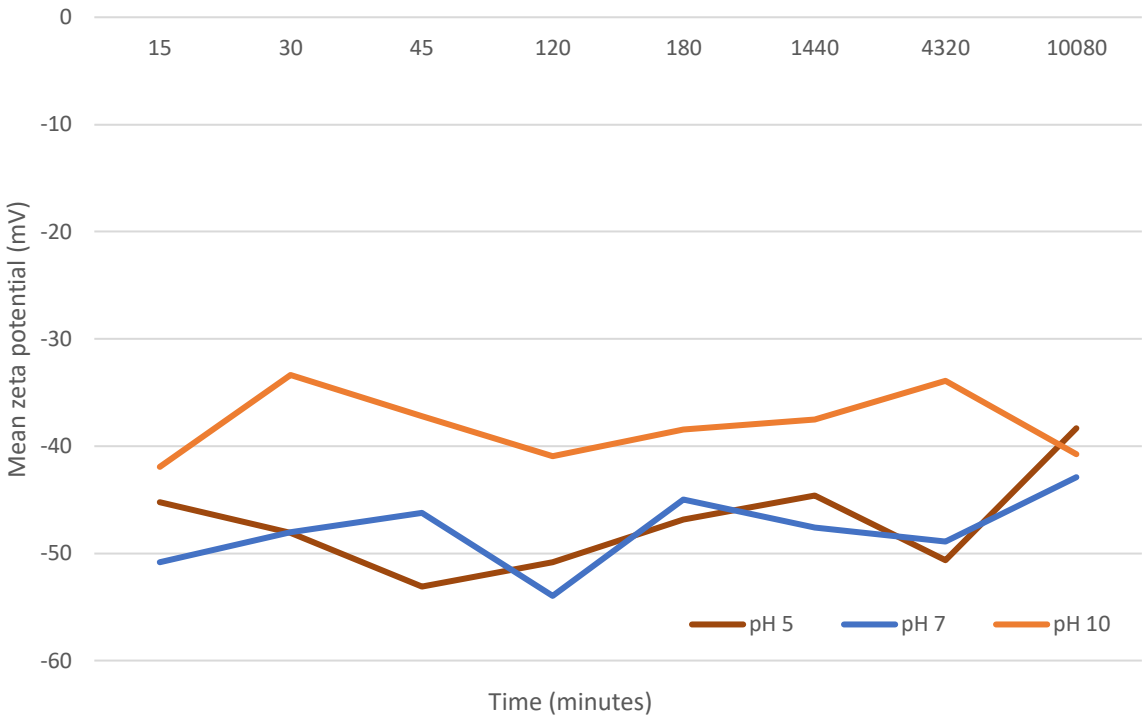

Figure 19: Mean zeta potential over time.

With a view to confirming the PSD provided by the dynamic light scattering, and for providing more structural information of the silica nanoparticles after diluting, the small angle x-ray was employed as Method 5. However, the were a number of challenges that had to be overcome before any useful data could be collected. By far the biggest challenge experienced was down to the sealing of the glass capillaries. Two alternate methods of doing this were tried but both were relatively unsuccessful at creating a strong enough seal to withstand the vacuum chamber of the instrument. Therefore, out of the 14 samples that were tested, only 2 were able to provide useful data.

The data collected via the small angle x-ray scattering instrument were for deionised water (used in the dilutions in Method 7) and a 1 vol% SiO_2 that had been diluted from the stock LUDOX silica via Method 7. The x-ray scatter data collected from the water sample was subtracted from the 1 vol% colloidal silica to obtain information regarding its size, shape and surface. As shown in Figures 20 and 21, the degree of 'scatter' obtained from the water sample, depicted as the intensity of contrast, was significantly less than that obtained from the colloidal silica sample. The reference water scatter data was subtracted from the silica scatter data and the results were processed using statistical techniques.

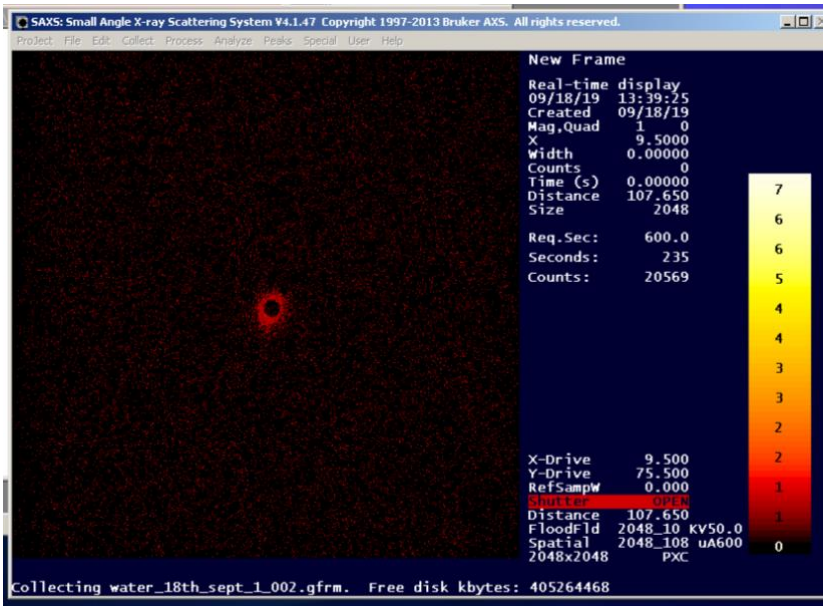

Figure 20: Low level scattering from water reference sample in the small angle x-ray employed as Method 6.

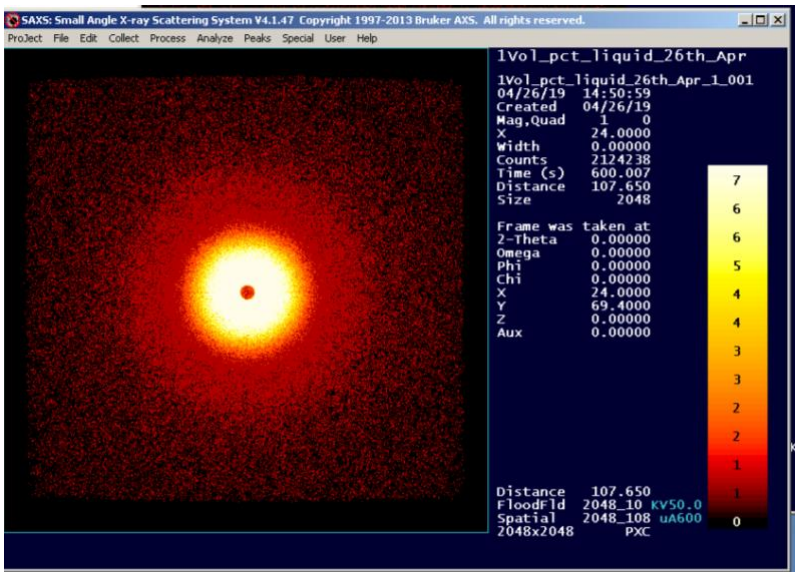

Figure 21: High level of scattering from a 1 vol% colloidal SiO_2 sample using a small angle x-ray

The distribution of lengths of the silica nanoparticles within the sample were plotted, as shown as Figure 22. The distribution of lengths within the sample gave a very clear bell curve. This indicates that the silica nanoparticle was highly spherical in structure suggesting that a large fraction of nanoparticles within the diluted dispersant were not aggregated to form irregular shapes. In addition to this, the Guinier plot (Figure 23) of the log of scattering intensity vs the

square of intensity gave a highly linear curve. This indicates that the sample was highly monodispersed, consisting of ~8 nm particles. This size information is in agreement with the dynamic light scattering measurements made.

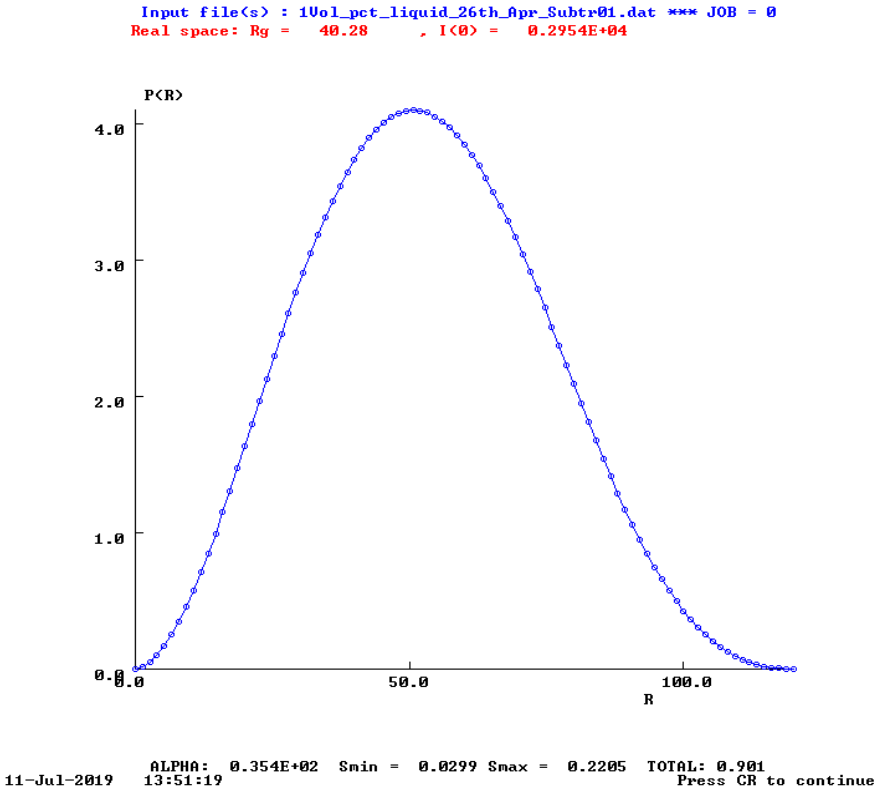

Figure 22: P-R function of 1 vol% colloidal silica.

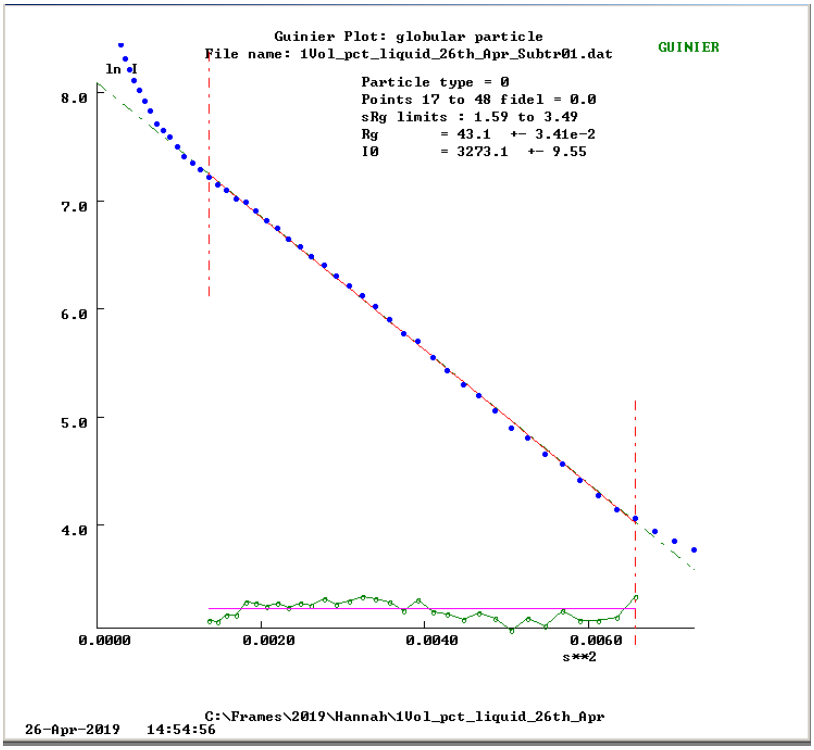

Figure 23: Guinier plot showing highly monodispersed SiO_2 NPs.

4.3 Summary

The particle size distribution of the diluted LUDOX silica was measured to be 5-20 nm (d. nm). These particle sizes are ideal for the next stage of the investigation involving the high frequency ultrasound imaging.

Limitations have arisen from the high failure rate of glass capillaries when placed under vacuum in the small angle x-ray. A possible recommendation for future work would be to improve this technique to allow for more easier usage.

Chapter 5: Results and discussion of the tissue mimic synthesis and the ultrasound measurements

5.1. Introduction

The diluted colloidal silica is to be set into a semi-solid gelatine phase so that it can be fully submerged into the ultrasound measurements tank. The concentrations of colloidal silica, prepared in Methods 1-4 for the incorporation into the tissue mimic were; 1, 2, 3, 4, 8, 15, and 20 vol%. During the incorporation into the tissue mimic, these concentrations were reduced to 0.2, 0.4, 0.65, 0.88, 1.75, 3.28 and 4.38 vol% respectively. On synthesis of the tissue mimic, the particle size distribution was assessed once more to ensure no significant increases in particle size are introduced, compromising its monodispersed properties.

The ultrasound attenuation data gained from the ultrasound measurements will be analysed in an attempt to identify any acoustic dependant behaviour that the nanoparticle may possess.

5.2 Results and discussion

Effects of temperature on the volume mean diameter (d. nm) of the silica nanoparticles was investigated using dynamic light scattering. The results from the measurements, shown in Figures 24 and 25 indicate that the heat energy applied to the colloidal system during tissue mimic synthesis will have little to no effect of the particle size distribution.

However, many challenges did arise in the making of the silica-gelatine samples. Higher concentrations of colloidal silica exhibited a high degree of compatibility with the gelatine. Although lower concentrations were able to be mixed within the gelatine relatively easily, the higher concentrations showed a great deal of resistance to mixing. The formation of significant amounts of bubbles, even without mixing, lead to foaming and rapid cooling when placed inside the vacuum oven. Although there many researches and tissue mimic developers that use gelatine and agar on a regular basis, little to no effort seems to have been made in characterising the size of particles that they employ within them. This suggests that the drastic change in viscosity is due to the molecular interactions between silica and gelatine. The sol-gel process is a well know nano synthesis process that manipulates the surface chemical reactions between gelatine molecules.

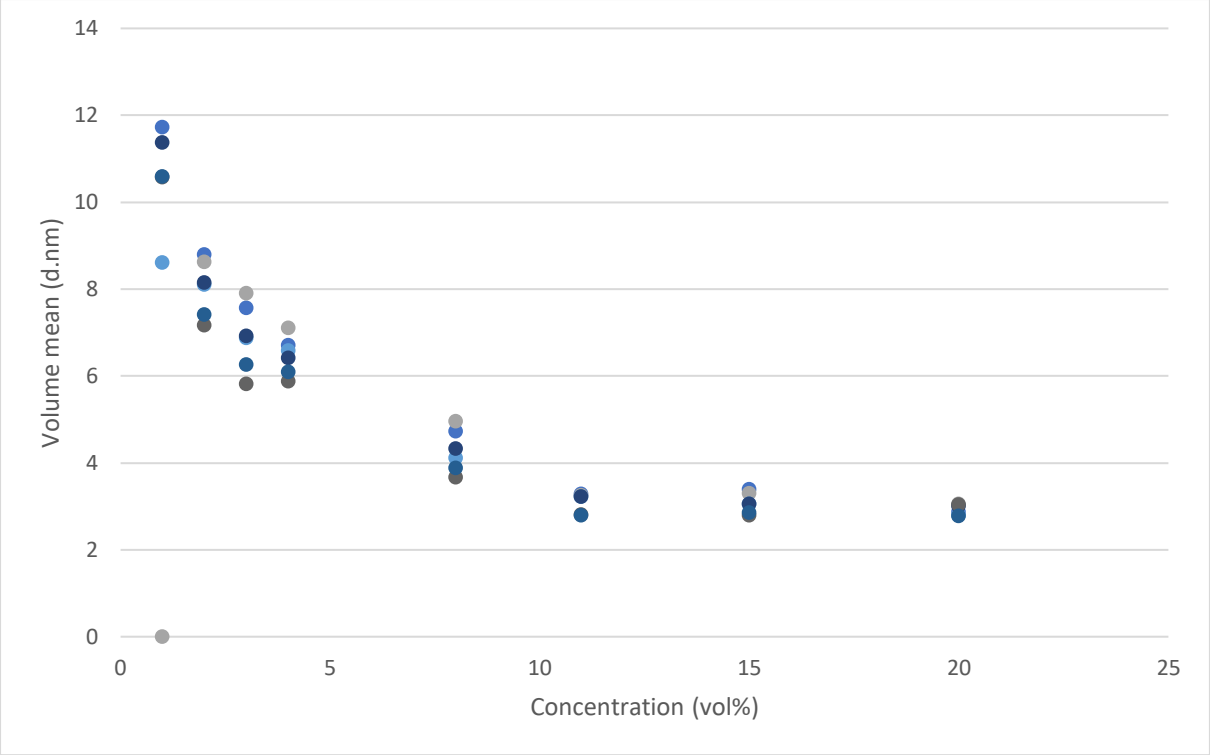

Figure 24: Particle size distribution of colloidal silica after heating to 55C.

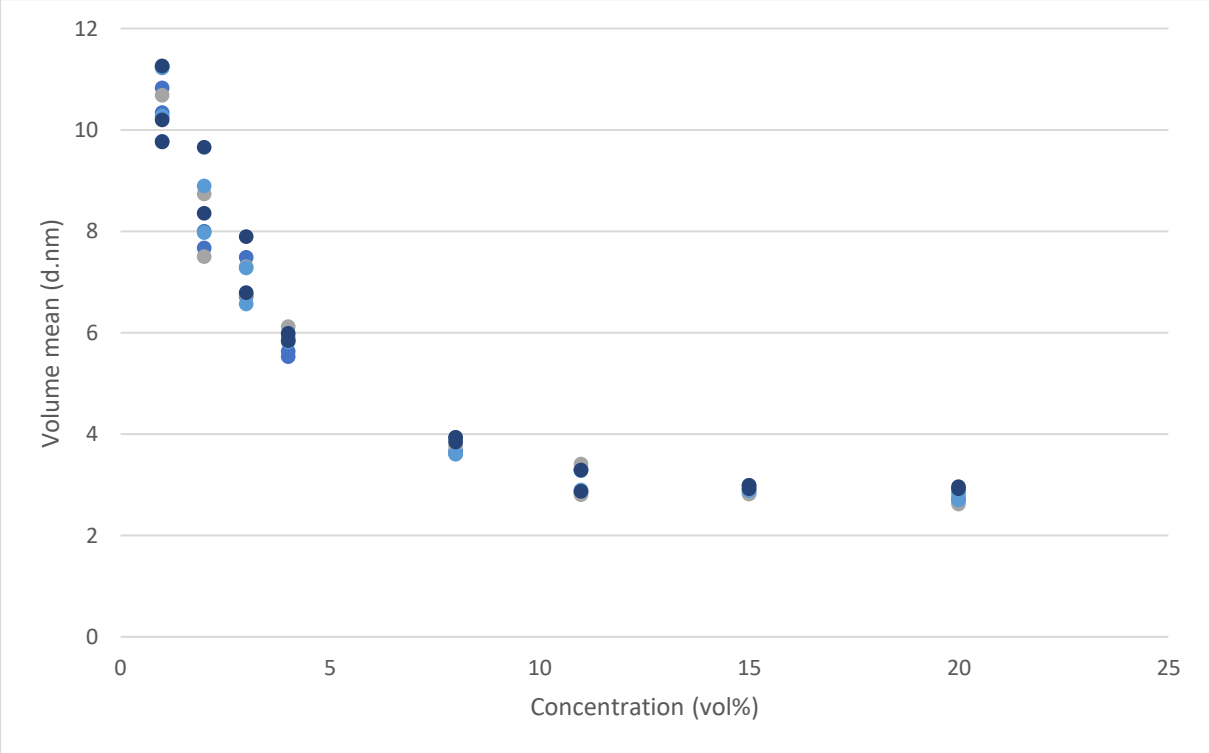

Figure 25: Particle size distribution of colloidal silica without any heat applied.

The dynamic light scattering measurements taken of the gelatine/silica solution (prepared via Method 8) gave very consistent narrow distributions with low zeta potential, as shown in Figure 26.

Temperature (°C):	55.0	**Zeta Runs:**	12
Count Rate (kcps):	87.2	**Measurement Position (mm):**	4.50
Cell Description:	Zeta dip cell	**Attenuator:**	8

		Mean (mV)	Area (%)	St Dev (mV)
Zeta Potential (mV):	-4.29	**Peak 1:** -4.29	100.0	3.02
Zeta Deviation (mV):	3.02	**Peak 2:** 0.00	0.0	0.00
Conductivity (mS/cm):	1.27	**Peak 3:** 0.00	0.0	0.00

Result quality : Good

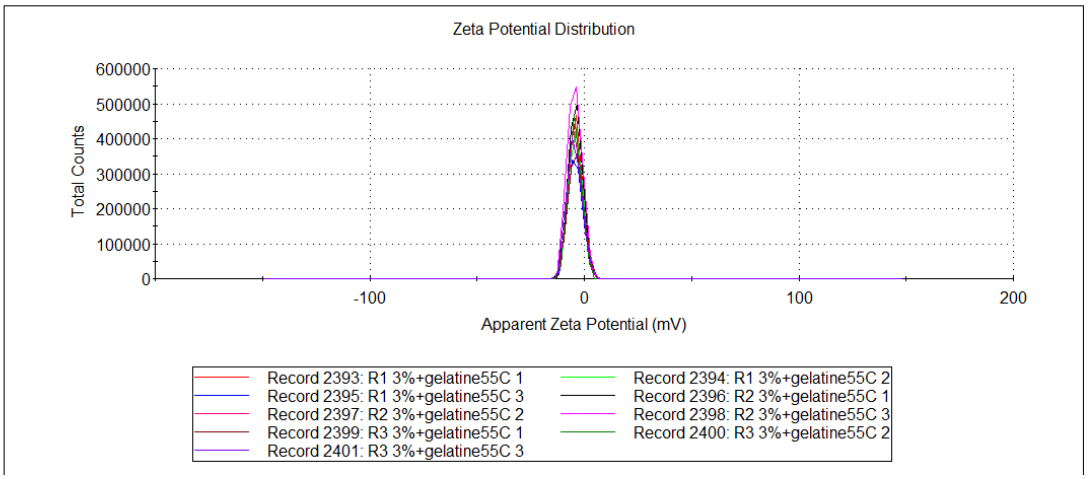

Figure 26: Zeta potential distribution of 3 vol% silica in gelatine.

In addition to this, the dynamic light scatterer was also able to identify a second population to that of the silica nanoparticles. As shown in Figure 27, the peak occurring at approximately 30 d. nm is one that is in line with the previous measurements taken of the silica in water as opposed to gelatine. The larger peak shown to the right of Figure 27 corresponds to a population with a volume mean size of approximately 1000 nm, can be identified as gelatine. Therefore, the silica nanoparticles within the tissue mimic can be characterised with a particle size distribution of 10-100 nm. This size of nanoparticle is in line with the objectives outlined at the beginning of this work.

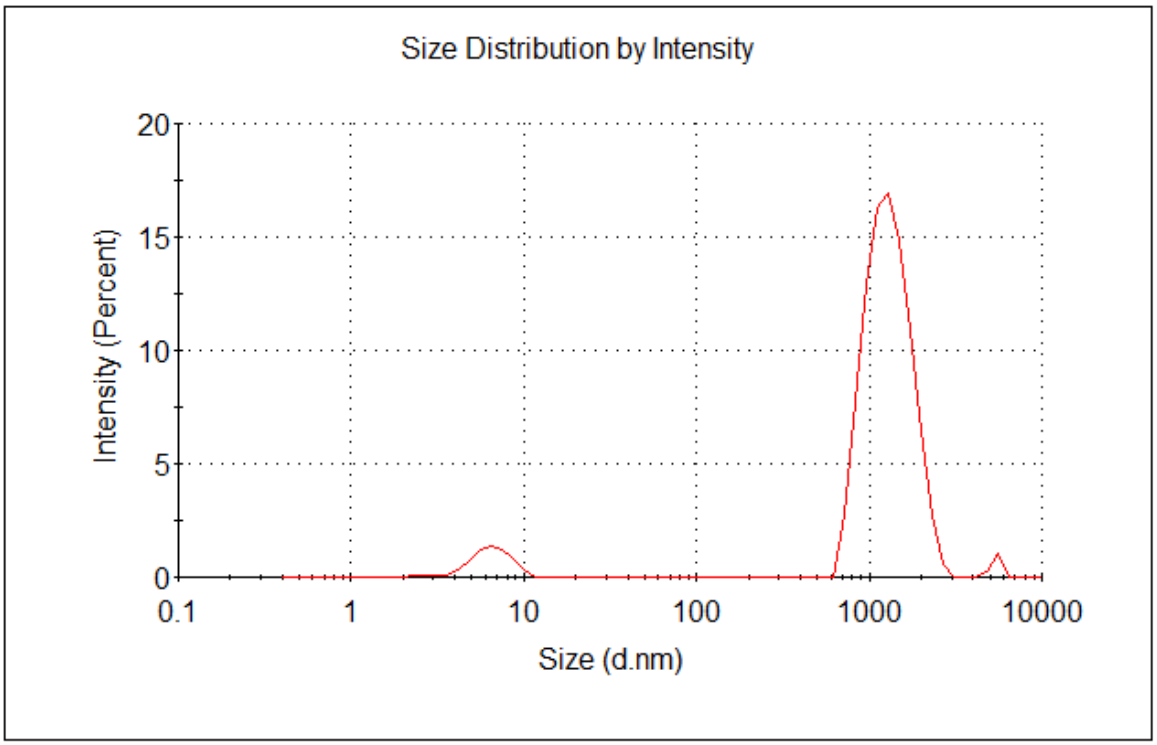

Figure 27: volume mean particles sizes of a co-population of SiO_2 and gelatine particles.

Although ultrasound attenuation is more accurately calculated by the difference between the front-face and back-face reflections, due to the high levels of noise experienced with the experimental setup as described in Method 9, the front and back-face reflections of the sample were unidentifiable. Therefore, the attenuation of acoustic energy through the sample was calculated by measuring the thickness of the samples by hand.

A plot of attenuation with increasing concentrations of silica, as a function of frequency is shown in Figure 28. Although the broadband transducer was able to extend below and above the frequencies show, the standard error associated with data points was significantly high therefore, they were removed from any data analysis.

Unsurprisingly, there was an overall increase in attenuation at higher frequencies and with increased concentration of nanoparticles. However, the concentrations used throughout these measurements are intentionally low. By demonstrating the ability to be highly attenuating at very low concentrations, enhances their ability to be detected at concentrations lower than their current toxicology profiles.

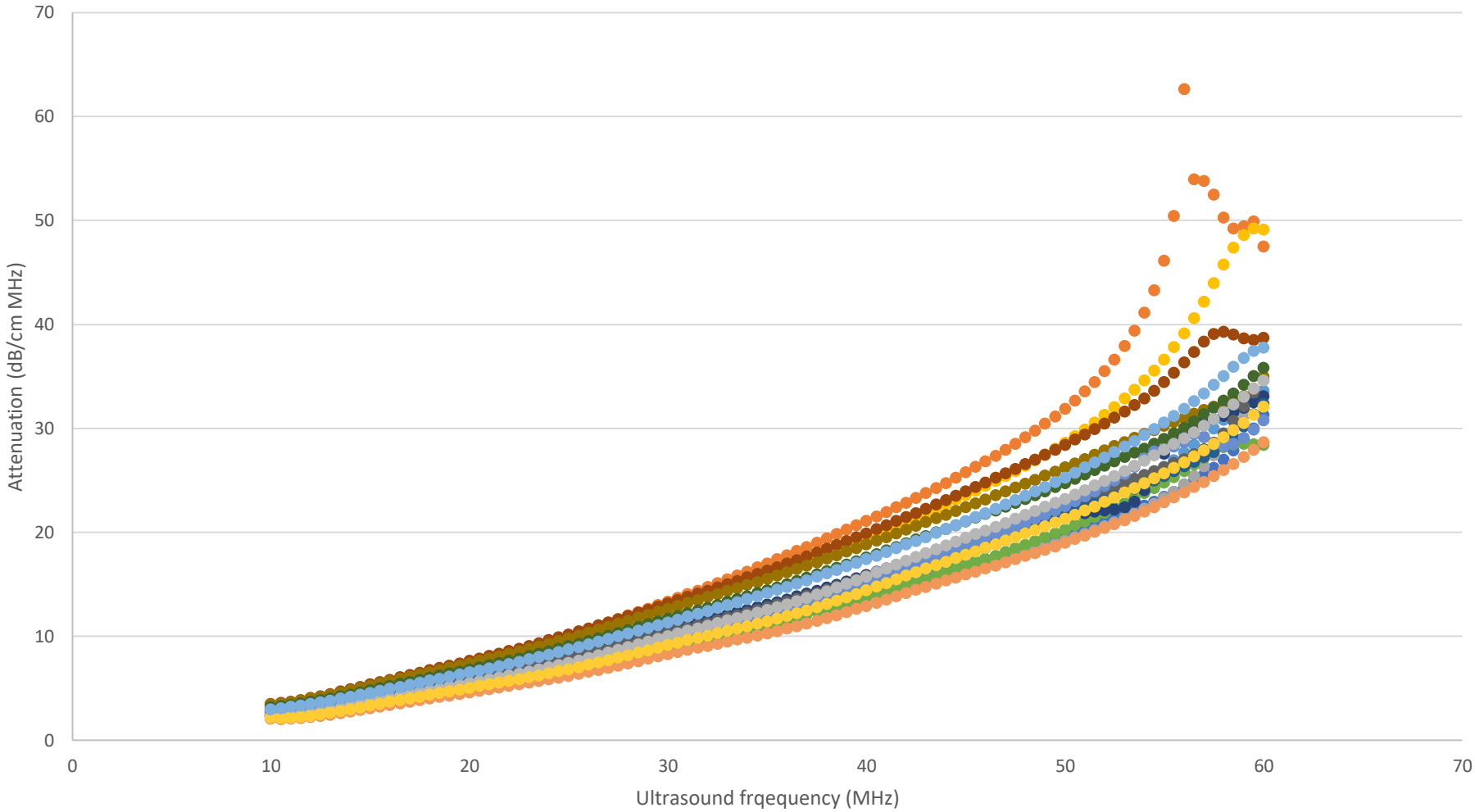

Figure 28: Acoustic attenuation with increasing silica nanoparticle concentration

By isolating the attenuation data associated with each particular frequency, a change in the attenuation curve with increasing silica concentration occurs at above 45 MHz (as shown in Figure 29). However, this particular frequency dependency of silica concentration can be seen more prominently in Figure 30. In Figure 30, the attenuation observed with a reference gelatine sample containing no nanoparticles was measures and subtracted from each of the samples containing silica concentrations. The subtraction of the reference enabled the attenuation due to silica nanoparticle to be seen more clearly. As shown, for concentrations between 2.5 and 4 vol%, the attenuation was significantly higher than that above or below this concentration. However, although the particle size distribution was assessed in this work, the particle distribution within the sample was not. For this type of acoustic dependency to be studied in more detail, particle size distribution as well as particle distribution would need to be fully assessed.

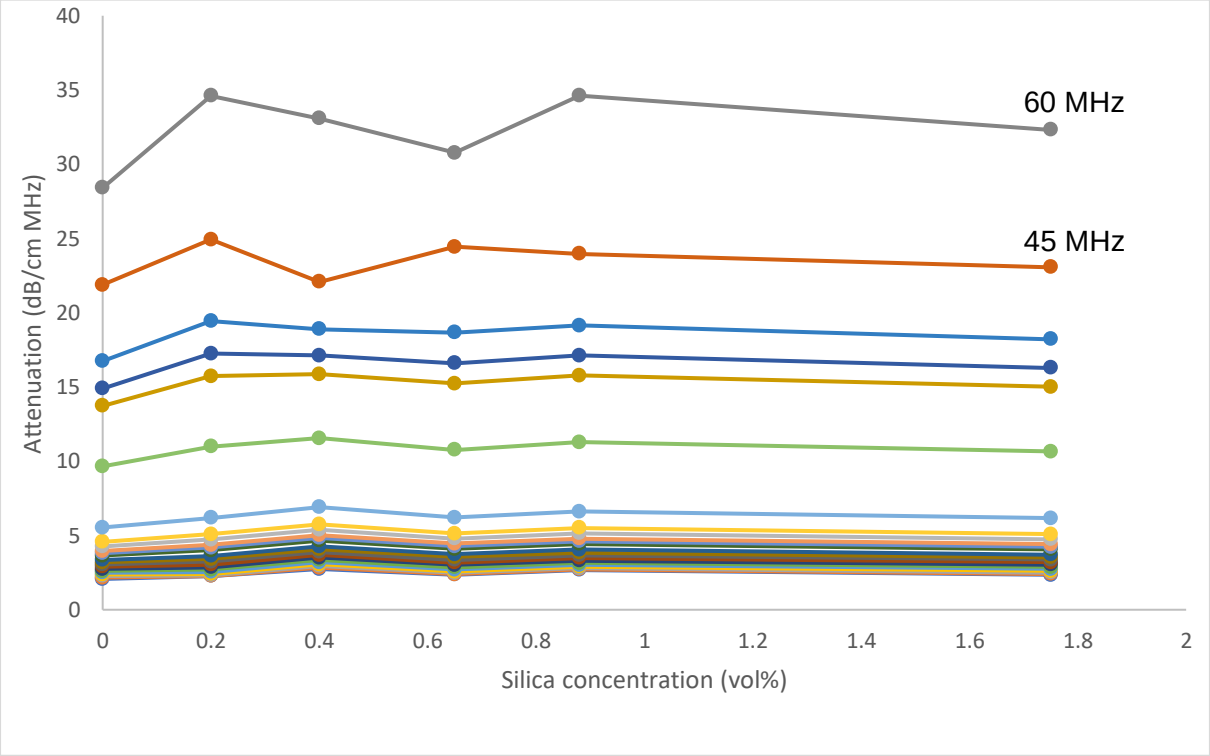

Figure 29: Attenuation of each frequency as a function of silica concentration

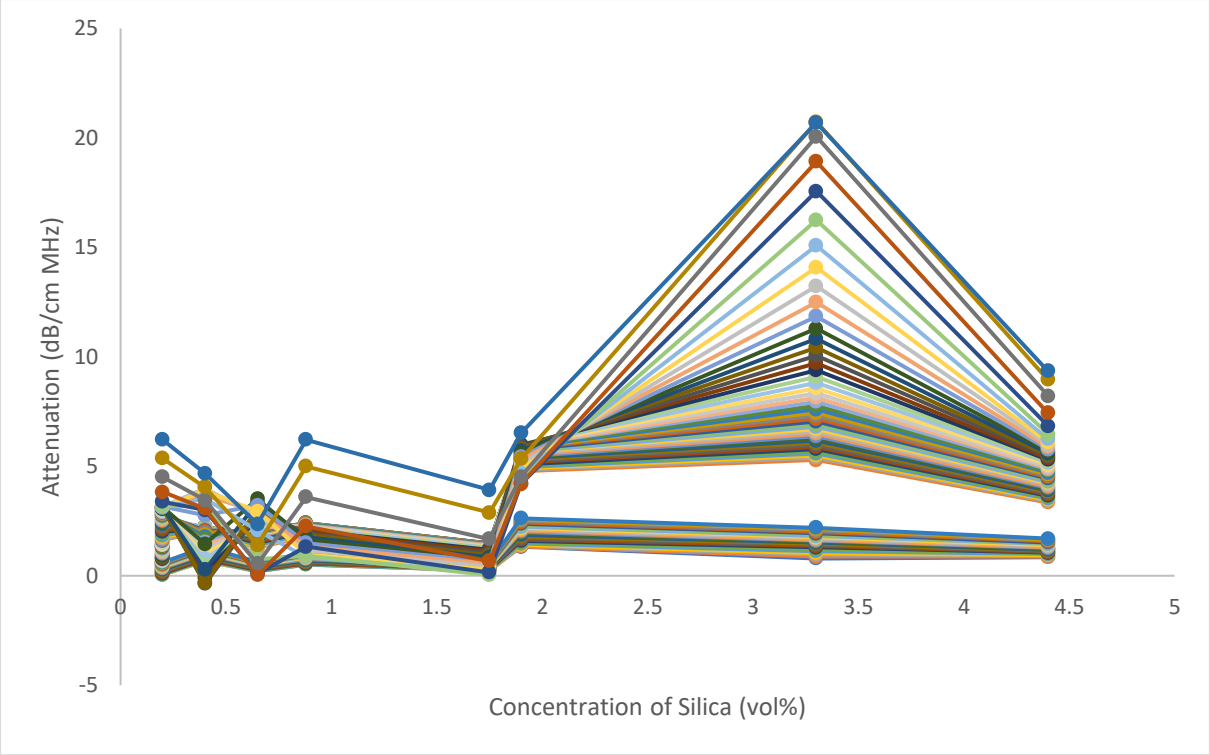

Figure 30: reference attenuation subtracted from sample attenuation and plotted as a function of silica concentration

5.3 Conclusion

The particle size distribution was characterised within the gelatine sample to have a mean size of 10-100nm. This size range meets one the objectives of the work. However, the incorporation of silica nanoparticles into gelatine-based tissue mimics has presented a number of challenges. A suggestion for future work would be to study the use of nanoparticles (10-100 nm) within tissue mimics with a view to developing a more reliable method for synthesis.

6.0 Conclusion

Nano-sized particles between 10-100nm were employed in this work to investigate the acoustic properties of a specific type nanoparticle material. The particle size distribution of the particles within a tissue mimic was characterised and used to implement a number of acoustic measurements. The ultrasounds attenuation data acquired did not show any direct link to a material specific property of the nanoparticle however, the development of the early stage experimental design carried out in this work was demonstrated to provide the acoustic data required for further investigations and future work in this area of research.

7.0 Recommendations for Future Work

In order to achieve an accousticly accurate tissue mimic with correct density and speed of sound, a concentration of 8 wt.% gelatine was used in this work. The viscosity of the gelatine-silica system produced via Method 7 was found to significantly increase with increasing concentration of colloidal silica used in the preparation. As a result, large volumes of air were able to become trapped within the sample. The air within the sample therefore significantly increasing the degree of noise experienced on collecting attenuation data via Method 9 and were therefore unable to be used. Therefore, the interactions between the gelatine and colloidal silica used in this work suggests that an alternative setting agent such as agar may be a better alternative for tissue mimic synthesis with colloidal silica NPs.

In addition to this, the introduction of nano and micron sized particles to more accurately represent the natural acoustic scatter signature of human tissue will enable more accurate and representative data to be collected.

Most of the samples prepared for the small angle x-ray data collection via Method 6 were unsuccessful and ruptured under the vacuum of the sample chamber. The glass capillaries used were sealed using two separate techniques however, both were found to be relatively unsuccessful. Further development of these techniques is required if particle information is to be acquired via this analytic technique.

The use of an additional analytical technique such as SEM may also be used to further support the dynamic light scattering data obtained in this work however, the use of a biological samples such as those containing gelatine or agar in an SEM may present its own limitations due to the risk of contaminating the equipment.

Further tissue mimic development as suggested above, in addition to particle size distribution mapping and particle size characterisation would enable more accurate attenuation data to be obtained with a view to further investigating the material specific acoustic properties of silica nano particles.

References

Abenojar, E. C., Nittayacharn, P., de Leon, A. C., Perera, R., Wang, Y., Bederman, I., & Exner, A. A. (2019). Effect of Bubble Concentration on the in Vitro and in Vivo Performance of Highly Stable Lipid Shell-Stabilized Micro- and Nanoscale Ultrasound Contrast Agents. *Langmuir, 35*(31), 10192-10202. doi:10.1021/acs.langmuir.9b00462

Abou-Elkacem, L., Bachawal, S. V., & Willmann, J. K. (2015). Ultrasound molecular imaging: Moving toward clinical translation. *Eur J Radiol, 84*(9), 1685-1693. doi:10.1016/j.ejrad.2015.03.016

Adekola, K., Rosen, S. T., & Shanmugam, M. (2012). Glucose transporters in cancer metabolism. *Curr Opin Oncol, 24*(6), 650-654. doi:10.1097/CCO.0b013e328356da72

Agide, F. D., Sadeghi, R., Garmaroudi, G., & Tigabu, B. M. (2018). A systematic review of health promotion interventions to increase breast cancer screening uptake: from the last 12 years. *Eur J Public Health, 28*(6), 1149-1155. doi:10.1093/eurpub/ckx231

Antoch, G., Freudenberg, L. S., Beyer, T., Bockisch, A., & Debatin, J. (2004). To Enhance or Not to Enhance? 18F-FDG and CT Contrast Agents in Dual-Modality 18F-FDG PET:CT. *The journal of Nuclear Medicine, 45*(1), 56-65.

Attia, A. B. E., Balasundaram, G., Moothanchery, M., Dinish, U. S., Bi, R., Ntziachristos, V., & Olivo, M. (2019). A review of clinical photoacoustic imaging: Current and future trends. *Photoacoustics, 16*, 100144. doi:10.1016/j.pacs.2019.100144

Bach, P. B., Brawley, O. W., & Silvestri, G. A. (2018). Low-dose CT for lung cancer screening. *The Lancet Oncology, 19*(3), e133-e134. doi:10.1016/s1470-2045(18)30117-7

Barua, D. (2018). A model-based analysis of tissue targeting efficacy of nanoparticles. *J R Soc Interface, 15*(140). doi:10.1098/rsif.2017.0787

Baur, A. D. J., Schwabe, J., Rogasch, J., Maxeiner, A., Penzkofer, T., Stephan, C., . . . Fischer, T. (2018). A direct comparison of contrast-enhanced ultrasound and dynamic contrast-enhanced magnetic resonance imaging for prostate cancer detection and prediction of aggressiveness. *Eur Radiol, 28*(5), 1949-1960. doi:10.1007/s00330-017-5192-2

Beiderwellen, K., Grueneisen, J., Ruhlmann, V., Buderath, P., Aktas, B., Heusch, P., . . . Umutlu, L. (2015). [(18)F]FDG PET/MRI vs. PET/CT for whole-body staging in patients with recurrent malignancies of the female pelvis: initial results. *Eur J Nucl Med Mol Imaging, 42*(1), 56-65. doi:10.1007/s00259-014-2902-8

Beiderwellen, K., Huebner, M., Heusch, P., Grueneisen, J., Ruhlmann, V., Nensa, F., . . . Lauenstein, T. C. (2014). Whole-body [(1)(8)F]FDG PET/MRI vs. PET/CT in the assessment of bone lesions in oncological patients: initial results. *Eur Radiol, 24*(8), 2023-2030. doi:10.1007/s00330-014-3229-3

Bertolotto, M., Bucci, S., Valentino, M., Curro, F., Sachs, C., & Cova, M. A. (2018). Contrast-enhanced ultrasound for characterizing renal masses. *Eur J Radiol, 105*, 41-48. doi:10.1016/j.ejrad.2018.05.015

Borg, R. E., & Rochford, J. (2018). Molecular Photoacoustic Contrast Agents: Design Principles & Applications. *Photochem Photobiol, 94*(6), 1175-1209. doi:10.1111/php.12967

Brown, R. W., Cheng, Y. N., Haacke, E. M., Thompson, M. R., & Venkatesan, R. (2014). *Magnetic resonance imaging: Physical principles and sequence design*. In.

Buccafusca, G., Proserpio, I., Tralongo, A. C., Rametta Giuliano, S., & Tralongo, P. (2019). Early colorectal cancer: diagnosis, treatment and survivorship care. *Crit Rev Oncol Hematol, 136*, 20-30. doi:10.1016/j.critrevonc.2019.01.023

Callister, M. E., & Janes, S. M. (2017). Defining the path: lung cancer CT screening in Europe. *Thorax, 72*(9), 778-779. doi:10.1136/thoraxjnl-2017-210268

Chen, K., & Chen, X. (2010). Design and Development of Molecular Imaging Probes *Current Topics in Medical Chemistry, 10*(12), 1227-1236. doi:10.2174/156802610791384225

Chong, W. K., Papadopoulou, V., & Dayton, P. A. (2018). Imaging with ultrasound contrast agents: current status and future. *Abdom Radiol (NY), 43*(4), 762-772. doi:10.1007/s00261-018-1516-1

Conversano, F., Greco, A., Casciaro, E., Casciaro, S., Mischi, M., Ragusa, A., & Lay-Ekuakille, A. (2011). Ultrasound Detection of Nanoparticle Contrast Agents for Multimodal Molecular Imaging. *2011 IEEE International Symposium on Medical Measurements and Applications*, 477-481. doi:10.1109/MeMeA.2011.5966742

Cucchetti, A., Cescon, M., Erroi, V., & Pinna, A. D. (2013). Cost-effectiveness of liver cancer screening. *Best Pract Res Clin Gastroenterol, 27*(6), 961-972. doi:10.1016/j.bpg.2013.08.021

Dang, X., Bardhan, N. M., Qi, J., Gu, L., Eze, N. A., Lin, C. W., . . . Belcher, A. M. (2019). Deep-tissue optical imaging of near cellular-sized features. *Sci Rep, 9*(1), 3873. doi:10.1038/s41598-019-39502-w

De Jong, N., Bouakaz, A., & Frinking, P. (2000). Harmonic Imaging for Ultrasound Contrast Agents. *Proceedings of the IEEE Ultrasonics Symposium, 2*, 1869-1876. doi:10.1109/ULTSYM.2000.921689

Debbage, P., & Jaschke, W. (2008). Molecular imaging with nanoparticles: giant roles for dwarf actors. *Histochem Cell Biol, 130*(5), 845-875. doi:10.1007/s00418-008-0511-y

Dommaschk, M., Grobner, J., Wellm, V., Hovener, J. B., Riedel, C., & Herges, R. (2019). Dendronised Ni(ii) porphyrins as photoswitchable contrast agents for MRI. *Phys Chem Chem Phys, 21*(44), 24296-24299. doi:10.1039/c9cp04156g

Du, D., Fu, H.-J., Ren, W.-w., Li, X.-L., & Guo, L.-H. (2019). PSA targeted dual-modality manganese oxide–mesoporous silica nanoparticles for prostate cancer imaging. *Biomedicine & Pharmacotherapy, 121*. doi:10.1016/j.biopha.2019.109614

Dukhin, A. S., & Goetz, P. J. (2010). *Characterization of Liquids, Nano- and Microparticulates, and Porous Bodies using Ultrasound* (2 ed.). Amsterdam: Elsevier.

Erfanzadeh, M., & Zhu, Q. (2019). Photoacoustic imaging with low-cost sources; A review. *Photoacoustics, 14*, 1-11. doi:10.1016/j.pacs.2019.01.004

Feinstein, S. B., Coll, B., Staub, D., Adam, D., Schinkel, A. F., ten Cate, F. J., & Thomenius, K. (2010). Contrast enhanced ultrasound imaging. *J Nucl Cardiol, 17*(1), 106-115. doi:10.1007/s12350-009-9165-y

Furrer, M. A., Spycher, S. C. J., Buttiker, S. M., Gross, T., Bosshard, P., Thalmann, G. N., . . . Roth, B. (2019). Comparison of the Diagnostic Performance of Contrast-enhanced Ultrasound with That of Contrast-enhanced Computed Tomography and Contrast-enhanced Magnetic Resonance Imaging in the Evaluation of Renal Masses: A Systematic Review and Meta-analysis. *Eur Urol Oncol*. doi:10.1016/j.euo.2019.08.013

Gastounioti, A., Conant, E. F., & Kontos, D. (2016). Beyond breast density: a review on the advancing role of parenchymal texture analysis in breast cancer risk assessment. *Breast Cancer Res, 18*(1), 91. doi:10.1186/s13058-016-0755-8

Gnyawali, V., Moon, B. U., Kieda, J., Karshafian, R., Kolios, M. C., & Tsai, S. S. H. (2017). Honey, I shrunk the bubbles: microfluidic vacuum shrinkage of lipid-stabilized microbubbles. *Soft Matter, 13*(22), 4011-4016. doi:10.1039/c7sm00128b

Goldman, L. W. (2007). Principles of CT: radiation dose and image quality. *J Nucl Med Technol, 35*(4), 213-225; quiz 226-218. doi:10.2967/jnmt.106.037846

Gong, P., Song, P., & Chen, S. (2018). Improved Contrast-Enhanced Ultrasound Imaging With Multiplane-Wave Imaging. *IEEE Trans Ultrason Ferroelectr Freq Control, 65*(2), 178-187. doi:10.1109/TUFFC.2017.2781190

Goodwin, J. S., Sheffield, K., Li, S., & Tan, A. (2016). Receipt of Cancer Screening Is a Predictor of Life Expectancy. *J Gen Intern Med, 31*(11), 1308-1314. doi:10.1007/s11606-016-3787-y

Guo, Y., Raghu, M., Durand, M., & Hooley, R. (2018). Retroareolar masses and intraductal abnormalities detected on screening ultrasound: can biopsy be avoided? *Br J Radiol, 91*(1090), 20170816. doi:10.1259/bjr.20170816

Hall, M. D., Schulthsiss, T. E., Farino, G., & Wong, J. Y. C. (2015). Increase in higher risk prostate cancer cases following new screening recommendations by the US Preventive Services Task Force (USPSTF). *Journal of Clinical Oncology, 33*(7), 143-143. doi:10.1200/jco.2015.33.7_suppl.143

Hatch, Q. M., Kniery, K. R., Johnson, E. K., Flores, S. A., Moeil, D. L., Thompson, J. J., . . . Steele, S. R. (2016). Screening or Symptoms? How Do We Detect Colorectal Cancer in an Equal Access Health Care System? *J Gastrointest Surg, 20*(2), 431-438. doi:10.1007/s11605-015-3042-6

Hawkes, N. (2019). Cancer survival data emphasise importance of early diagnosis. *BMJ, 364*, l408. doi:10.1136/bmj.l408

Ho, C. J., Balasundaram, G., Driessen, W., McLaren, R., Wong, C. L., Dinish, U. S., . . . Olivo, M. (2014). Multifunctional photosensitizer-based contrast agents for photoacoustic imaging. *Sci Rep, 4*, 5342. doi:10.1038/srep05342

IARC. (2018). Latest global cancer data. Retrieved from https://www.who.int/cancer/PRGlobocanFinal.pdf

Iyer, A. K., Khaled, G., Fang, J., & Maeda, H. (2006). Exploiting the enhanced permeability and retention effect for tumor targeting. *Drug Discov Today, 11*(17-18), 812-818. doi:10.1016/j.drudis.2006.07.005

Kamal, R., Hamed, S., Mansour, S., Mounir, Y., & Abdel Sallam, S. (2018). Ovarian cancer screening-ultrasound; impact on ovarian cancer mortality. *Br J Radiol, 91*(1090), 20170571. doi:10.1259/bjr.20170571

Kavitha, M. S., Shanthini, J., & Sabitha, R. (2019). ECM-CSD: An Efficient Classification Model for Cancer Stage Diagnosis in CT Lung Images Using FCM and SVM Techniques. *J Med Syst, 43*(3), 73. doi:10.1007/s10916-019-1190-z

Kuhl, C. K. (2018). Abbreviated breast MRI for screening women with dense breast: the EA1141 trial. *Br J Radiol, 91*(1090), 20170441. doi:10.1259/bjr.20170441

Kummer, T., Oh, L., Phelan, M. B., Huang, R. D., Nomura, J. T., & Adhikari, S. (2018). Emergency and critical care applications for contrast-enhanced ultrasound. *Am J Emerg Med, 36*(7), 1287-1294. doi:10.1016/j.ajem.2018.04.044

LeVine, H. (2010). *Medical imaging* (1 ed.). Santa Barbara: Greenwood.

Li, J., Ling, W., Chen, S., Ma, L., Yang, L., Lu, Q., & Luo, Y. (2019). The interreader agreement and validation of contrast-enhanced ultrasound liver imaging reporting and data system. *Eur J Radiol, 120*, 108685. doi:10.1016/j.ejrad.2019.108685

Li, X., Wang, D., Ran, H., Hao, L., Cao, Y., Ao, M., . . . Li, P. (2018). A preliminary study of photoacoustic/ultrasound dual-mode imaging in melanoma using MAGE-targeted gold nanoparticles. *Biochem Biophys Res Commun, 502*(2), 255-261. doi:10.1016/j.bbrc.2018.05.155

Li, Y., Ma, J., Heath Martin, K., Yu, M., Ma, T., Dayton, P. A., . . . Zhou, Q. (2016). An Integrated System for Superharmonic Contrast-Enhanced Ultrasound Imaging: Design and Intravascular Phantom Imaging Study. *Transactions on Biomedical Engineering, 63*(9), 1933-1943.

Liao, W., Lei, P., Pan, J., Zhang, C., Sun, X., Zhang, X., . . . Sun, S. K. (2019). Bi-DTPA as a high-performance CT contrast agent for in vivo imaging. *Biomaterials, 203*, 1-11. doi:10.1016/j.biomaterials.2019.03.001

Lim, A. (2019). Can CEUS help stage breast cancer? *Ultrasound in Medicine & Biology, 45*, S43-S44. doi:10.1016/j.ultrasmedbio.2019.07.553

Lin, E., & Alessio, A. (2009). What are the basic concepts of temporal, contrast, and spatial resolution in cardiac CT? *J Cardiovasc Comput Tomogr, 3*(6), 403-408. doi:10.1016/j.jcct.2009.07.003

Marcelo, G. A., Lodeiro, C., Capelo, J. L., Lorenzo, J., & Oliveira, E. (2020). Magnetic, fluorescent and hybrid nanoparticles: From synthesis to application in biosystems. *Materials Science and Engineering: C, 106*. doi:10.1016/j.msec.2019.110104

Martinez, H. P., Kono, Y., Blair, S. L., Sandoval, S., Wang-Rodriguez, J., Mattrey, R. F., . . . Trogler, W. C. (2010). Hard shell gas-filled contrast enhancement particles for colour Doppler ultrasound imaging of tumors. *Medchemcomm, 1*(4), 266-270. doi:10.1039/c0md00139b

Massoud, T. F., & Gambhir, S. S. (2003). Molecular imaging in living subjects: seeing fundamental biological processes in a new light. *Genes and Developement, 17*(5), 545-580. doi:10.1101/gad.1047403

McNamara, K., & Tofail, S. A. M. (2016). Nanoparticles in biomedical applications. *Advances in Physics: X, 2*(1), 54-88. doi:10.1080/23746149.2016.1254570

Melany, M., & Chen, S. (2017). Thyroid Cancer: Ultrasound Imaging and Fine-Needle Aspiration Biopsy. *Endocrinol Metab Clin North Am, 46*(3), 691-711. doi:10.1016/j.ecl.2017.04.011

Menigot, S., & Girault, J. M. (2016). Optimization of contrast resolution by genetic algorithm in ultrasound tissue harmonic imaging. *Ultrasonics, 71*, 231-244. doi:10.1016/j.ultras.2016.06.022

Metin, C. O., Baran, J. R., Jr., & Nguyen, Q. P. (2012). Adsorption of surface functionalized silica nanoparticles onto mineral surfaces and decane/water interface. *J Nanopart Res, 14*(11), 1246. doi:10.1007/s11051-012-1246-1

Miranda, D. A., & Pertuz, S. (2019). Field cancerization in the understanding of parenchymal analysis of mammograms for breast cancer risk assessment. *Med Hypotheses, 136*, 109511. doi:10.1016/j.mehy.2019.109511

Molinos, C., Sasser, T., Salmon, P., Gsell, W., Viertl, D., Massey, J. C., . . . Heidenreich, M. (2019). Low-Dose Imaging in a New Preclinical Total-Body PET/CT Scanner. *Front Med (Lausanne), 6*, 88. doi:10.3389/fmed.2019.00088

Morabito, R., Alafaci, C., Pergolizzi, S., Pontoriero, A., Iati, G., Bonanno, L., . . . Granata, F. (2019). DCE and DSC perfusion MRI diagnostic accuracy in the follow-up of primary and metastatic intra-axial brain tumors treated by radiosurgery with cyberknife. *Radiat Oncol, 14*(1), 65. doi:10.1186/s13014-019-1271-7

Mori, N., Pineda, F. D., Tsuchiya, K., Mugikura, S., Takahashi, S., Karczmar, G. S., & Abe, H. (2018). Fast Temporal Resolution Dynamic Contrast-Enhanced MRI: Histogram Analysis Versus Visual Analysis for Differentiating Benign and Malignant Breast Lesions. *AJR Am J Roentgenol, 211*(4), 933-939. doi:10.2214/AJR.17.19225

Mortimore, G., & Mayes, J. P. (2019). Abdominal ultrasound scans for diagnostic imaging of the liver. *Gastrointestinal Nursing, 17*(6).

Muhi, A., Ichikawa, T., Motosugi, U., Sou, H., Nakajima, H., Sano, K., . . . Araki, T. (2011). Diagnosis of colorectal hepatic metastases: comparison of contrast-enhanced CT, contrast-enhanced US, superparamagnetic iron oxide-enhanced MRI, and gadoxetic acid-enhanced MRI. *J Magn Reson Imaging, 34*(2), 326-335. doi:10.1002/jmri.22613

Mulvana, H., Browning, R. J., Luan, Y., de Jong, N., Tang, M. X., Eckersley, R. J., & Stride, E. (2017). Characterization of Contrast Agent Microbubbles for Ultrasound Imaging and Therapy Research. *IEEE Trans Ultrason Ferroelectr Freq Control, 64*(1), 232-251. doi:10.1109/TUFFC.2016.2613991

Na, H. B., Song, I. C., & Hyeon, T. (2009). Inorganic Nanoparticles for MRI Contrast Agents. *Advanced Materials, 21*(21), 2133-2148. doi:10.1002/adma.200802366

NHS. (2018). Diagnostic Imaging Dataset: Annual Statistical Release. Retrieved from https://www.england.nhs.uk/statistics/statistical-work-areas/diagnostic-imaging-dataset/diagnostic-imaging-dataset-2017-18-data/

Obaro, A. E., Burling, D. N., & Plumb, A. A. (2018). Colon cancer screening with CT colonography: logistics, cost-effectiveness, efficiency and progress. *Br J Radiol, 91*(1090), 20180307. doi:10.1259/bjr.20180307

Parisi, M. T., Bermo, M. S., Alessio, A. M., Sharp, S. E., Gelfand, M. J., & Shulkin, B. L. (2017). Optimization of Pediatric PET/CT. *Semin Nucl Med, 47*(3), 258-274. doi:10.1053/j.semnuclmed.2017.01.002

Park, C.-S., Kim, J.-W., Cho, S., & Seo, D.-c. (2016). A high resolution approach for nonlinear sub-harmonic imaging. *NDT & E International, 79*, 114-122. doi:10.1016/j.ndteint.2016.01.001

Pasoglou, V., Michoux, N., Larbi, A., Van Nieuwenhove, S., & Lecouvet, F. (2018). Whole Body MRI and oncology: recent major advances. *Br J Radiol, 91*(1090), 20170664. doi:10.1259/bjr.20170664

Pellow, C., Goertz, D. E., & Zheng, G. (2018). Breaking free from vascular confinement: status and prospects for submicron ultrasound contrast agents. *Wiley Interdiscip Rev Nanomed Nanobiotechnol, 10*(4), e1502. doi:10.1002/wnan.1502

Perera, R. H., Wu, H., Peiris, P., Hernandez, C., Burke, A., Zhang, H., & Exner, A. A. (2017). Improving performance of nanoscale ultrasound contrast agents using N,N-diethylacrylamide stabilization. *Nanomedicine, 13*(1), 59-67. doi:10.1016/j.nano.2016.08.020

Poustchi, H., Farrell, G. C., Strasser, S. I., Lee, A. U., McCaughan, G. W., & George, J. (2011). Feasibility of conducting a randomized control trial for liver cancer screening: is a randomized controlled trial for liver cancer screening feasible or still needed? *Hepatology, 54*(6), 1998-2004. doi:10.1002/hep.24581

Ronot, M., Pommier, R., Dioguardi Burgio, M., Purcell, Y., Nahon, P., & Vilgrain, V. (2018). Hepatocellular carcinoma surveillance with ultrasound-cost-effectiveness, high-risk populations, uptake. *Br J Radiol, 91*(1090), 20170436. doi:10.1259/bjr.20170436

Rowe, M. E., Osorio, M., Likhterov, I., & Urken, M. L. (2017). Evaluation of ultrasound reporting for thyroid cancer diagnosis and surveillance. *Head Neck, 39*(9), 1756-1760. doi:10.1002/hed.24825

Ruoslahti, E. (2012). Peptides as Targeting Elements and Tissue Penetration Devices for Nanoparticles. *Advanced Materials, 24*(28), 3747-3756. doi:10.1002/adma.201200454

Ryu, J. H., Shin, M., Kim, S. A., Lee, S., Kim, H., Koo, H., . . . Kim, K. (2013). In vivo fluorescence imaging for cancer diagnosis using receptor-targeted epidermal growth factor-based nanoprobe. *Biomaterials, 34*(36), 9149-9159. doi:10.1016/j.biomaterials.2013.08.026

Saif, M. W., Tzannou, I., Makrilia, N., & Syrigos, K. (2010). Role and Cost Effectiveness of PET:CT in Management of Patients with Cancer. *Yale Journal of Biology and Medicine, 83*, 53-65.

Satir, S., & Degertekin, F. L. (2016). Phase and Amplitude Modulation Methods for Nonlinear Ultrasound Imaging With CMUTs. *IEEE Trans Ultrason Ferroelectr Freq Control, 63*(8), 1086-1092. doi:10.1109/TUFFC.2016.2557621

Schlemmer, H. P. (2009). Basic Principles of Mri. *Radiotherapy and Oncology, 92*. doi:10.1016/s0167-8140(12)72595-1

Shah, M. R., Imran, M., & Ullah, S. (2019). *Metal Nanoparticles for Drug Delivery and Diagnostic Applications*. Amsterdam: Elsevier.

Sharma, P., Brown, S. C., Bengtsson, N., Zhang, Q., Walter, G. A., Grobmyer, S. R., . . . Moudgil, B. M. (2008). Gold-Speckled Multimodal Nanoparticles for Noninvasive Bioimaging. *American Chemical Society, 20*(19), 6087-6094. doi:10.1021/cm801020s

Shobaki, N., Sato, Y., & Harashima, H. (2018). Mixing lipids to manipulate the ionization status of lipid nanoparticles for specific tissue targeting. *Int J Nanomedicine, 13*, 8395-8410. doi:10.2147/IJN.S188016

Smeenge, M., Tranquart, F., Mannaerts, C. K., Reijke, T. M., Vijver, M. J., Languna, M. P., . . . Wijkstra, H. (2017). First-in-Human Ultrasound Molecular Imaging With a VEGFR2-Specific Ultrasound Molecular Contrast Agent (BR55) in Prostate Cancer: A Safety and Feasibility Pilot Study. *Investigative radiology, 52*, 419-427. doi:10.1097/RLI.0000000000000362

Smith, E. A., Dillman, J. R., Goodsitt, M. M., Christodoulou, E. G., Keshavarzi, N., & Strouse, P. J. (2014). Model-based iterative reconstruction: Effect on Patient Radiation Dose and Image Quality in Pediatric Body CT1. *Radiology, 270*(2), 526-534.

Son, S., Min, H. S., You, D. G., Kim, B. S., & Kwon, I. C. (2014). Echogenic nanoparticles for ultrasound technologies: Evolution from diagnostic imaging modality to multimodal theranostic agent. *Nano Today, 9*(4), 525-540. doi:10.1016/j.nantod.2014.06.002

Song, R., Peng, C., Xu, X., Wang, J., Yu, M., Hou, Y., . . . Yao, S. (2018). Controllable Formation of Monodisperse Polymer Microbubbles as Ultrasound Contrast Agents. *ACS Appl Mater Interfaces, 10*(17), 14312-14320. doi:10.1021/acsami.7b17258

Sulheim, E., Kim, J., van Wamel, A., Kim, E., Snipstad, S., Vidic, I., . . . de Lange Davies, C. (2018). Multi-modal characterization of vasculature and nanoparticle accumulation in five tumor xenograft models. *J Control Release, 279*, 292-305. doi:10.1016/j.jconrel.2018.04.026

Sztandera, K., Gorzkiewicz, M., & Klajnert-Maculewicz, B. (2019). Gold Nanoparticles in Cancer Treatment. *Mol Pharm, 16*(1), 1-23. doi:10.1021/acs.molpharmaceut.8b00810

Vallet-Regi, M., Colilla, M., Izquierdo-Barba, I., & Manzano, M. (2017). Mesoporous Silica Nanoparticles for Drug Delivery: Current Insights. *Molecules, 23*(1). doi:10.3390/molecules23010047

Wang, L. Y., & Zheng, S. S. (2019). Advances in low-frequency ultrasound combined with microbubbles in targeted tumor therapy. *J Zhejiang Univ Sci B, 20*(4), 291-299. doi:10.1631/jzus.B1800508

Wang, T., Ni, M., Luo, Z., Shou, C., & Cen, K. (2012). Viscosity and aggregation structure of nanocolloidal dispersions. *Chinese Science Bulletin, 57*(27), 3644-3651. doi:10.1007/s11434-012-5150-y

Wang, Y., Chen, H., Li, N., Ren, J., Zhang, K., Dai, M., & He, J. (2019). Ultrasound for Breast Cancer Screening in High-Risk Women: Results From a Population-Based Cancer Screening Program in China. *Front Oncol, 9*, 286. doi:10.3389/fonc.2019.00286

WHO. (2008). Cancer: Key statistics. Retrieved from https://www.who.int/cancer/resources/keyfacts/en/

Wilhelm, S., Tavares, A. J., Dai, Q., Ohta, S., Audet, J., Dvorak, H. F., & Chan, W. C. W. (2016). Analysis of nanoparticle delivery to tumours. *Nature Reviews Materials, 1*(5). doi:10.1038/natrevmats.2016.14

Willmann, J. K., CBonomo, L., Testa, A. C., Rinaldi, P., Rindi, G., Valluru, K. S., . . . Gambhir, S. S. (2017). Ultrasound Molecular Imaging With BR55 in Patients With Breast and Ovarian Lesions: First-in-Human Results. *Journal of Clinical Oncology, 35*(19), 2133-2140. doi:10.1200/JCO

10.1200/JCO.2016

Witte, R. S., Karunakaran, C., Zuniga, A. N., Schmitz, H., & Arif, H. (2018). Frontiers of cancer imaging and guided therapy using ultrasound, light, and microwaves. *Clin Exp Metastasis, 35*(5-6), 413-418. doi:10.1007/s10585-018-9923-9

Wolbarst, A. B., Capasso, P., & Wyant, A. R. (2013). *Medical imaging: Essentials for physicians* (1 ed.). Hoboken: Wiley.

Wu, D., Huang, L., Jiang, M. S., & Jiang, H. (2014). Contrast Agents for photoacoustic and Thermoacoustic Imaging: A Review. *International Journal of Molecular Sciences, 15*, 23616-23639. doi:10.3390/ijms151223616

Zhang, L., Zhang, L., Wang, H., Chen, L., & Sui, G. (2019). Diagnostic performance of contrast-enhanced ultrasound and magnetic resonance imaging for detecting colorectal liver metastases: A systematic review and meta-analysis. *Dig Liver Dis, 51*(9), 1241-1248. doi:10.1016/j.dld.2019.06.004

Zlitni, A., & Gambhir, S. S. (2018). Molecular imaging agents for ultrasound. *Curr Opin Chem Biol, 45*, 113-120. doi:10.1016/j.cbpa.2018.03.017